Myosin lever arm directs collective motion on cellular actin network

Rizal F. Hariadi[a], Mario Cale[b], and Sivaraj Sivaramakrishnan[a,b,c,1]

[a]Department of Cell and Developmental Biology, [b]Department of Biophysics, and [c]Department of Biomedical Engineering, University of Michigan, Ann Arbor, MI 48109

Edited by James A. Spudich, Stanford University School of Medicine, Stanford, CA, and approved February 7, 2014 (received for review August 22, 2013)

The molecular motor myosin teams up to drive muscle contraction, membrane traffic, and cell division in biological cells. Myosin function in cells emerges from the interaction of multiple motors tethered to a scaffold, with surrounding actin filaments organized into 3D networks. Despite the importance of myosin function, the influence of intermotor interactions on collective motion remains poorly understood. In this study, we used precisely engineered myosin assemblies to examine emergence in collective myosin movement. We report that tethering multiple myosin VI motors, but not myosin V motors, modifies their movement trajectories on keratocyte actin networks. Single myosin V and VI dimers display similar skewed trajectories, albeit in opposite directions, when traversing the keratocyte actin network. In contrast, tethering myosin VI motors, but not myosin V motors, progressively straightens the trajectories with increasing myosin number. Trajectory shape of multimotor scaffolds positively correlates with the stiffness of the myosin lever arm. Swapping the flexible myosin VI lever arm for the relatively rigid myosin V lever increases trajectory skewness, and vice versa. A simplified model of coupled motor movement demonstrates that the differences in flexural rigidity of the two myosin lever arms is sufficient to account for the differences in observed behavior of groups of myosin V and VI motors. In accordance with this model trajectory, shapes for scaffolds containing both myosin V and VI are dominated by the myosin with a stiffer lever arm. Our findings suggest that structural features unique to each myosin type may confer selective advantages in cellular functions.

motor proteins | single molecule biophysics | synthetic biology | DNA nanotechnology | collective decision-making

Collective motion of a group is often influenced by interactions between individual entities, leading to emergence not evident in the individual (1). Stellar streaming (2), segregation of pedestrian traffic (3), and the migration of biological cells (4) are examples that span the size spectrum. Stellar streaming emerges from the gravitational interactions between ancient orbiting stars and the entire galaxy (2). Pedestrians adjust their movements on the basis of visual cues, such as the distance to an obstruction, giving rise to spontaneous unidirectional lanes for faster migration through a crowd (3). In migrating cells, local remodeling of the cytoskeleton is sufficient to effect global changes in the shape and persistence of movement direction (4). Although the importance of emergence in nature is generally appreciated, defining the underlying parameters that influence collective motion remains a challenge. In biology, the cell is packed with proteins that undergo relatively weak interactions in spatially segregated groups that give rise to large-scale intracellular structure, cellular migration, and tissue-level phenomena such as muscle motion and memory. Despite its importance, studies of emergence in cell biology have been limited, until recently, by the lack of engineered systems at the nanoscale.

The cellular function of the myosin family of cytoskeletal motors emerges from the interaction of several myosins tethered to a scaffold with the surrounding actin filaments (5). Actin architecture in cells is inherently 2D or 3D, as witnessed in dense cortical meshworks (6), filament bundles in filopodia (7), and parallel hexagonal arrays in muscle sarcomeres (8, 9). In concert, collective myosin function in cells varies with actin organization. Whereas multiple membrane-tethered myosin VI motors interact with actin bundles to anchor stereocilia (10), myosin VI motors on uncoated endosomes are necessary for their timely transport through a dense actin cortex, and myosin VI localized on the Golgi functions as a tether to maintain organelle shape and size (11). In muscle, the collective interaction of myosins patterned on rod-like structures with actin filaments arranged in hexagonal lattices forms the molecular basis of muscle contraction (8, 9). In each of these instances, the contribution of intermotor interactions, patterned in different geometric configurations, on collective myosin remains unexplored.

Myosin function in a cellular context has been examined either as the interaction of single molecules with cellular actin networks (12, 13) or the movement of two motors tethered together on single actin filaments (14, 15). Single myosin studies have identified unique structural features in the protein that select for processive movement on certain actin topologies (13, 16, 17). Tethering two identical myosins enhances travel distance along single actin filaments, but at lower speeds (15). Tethering myosins that move toward the opposite ends of an actin filament results in unidirectional motion, with the two motors coordinating their stepping movements (14). The intermotor interactions in these systems have also been investigated with theoretical approaches that, combined with experimental observations, have yielded insights into the underlying parameters that govern collective movement (18–23). Although there have been studies on the collective movement of myosins on cellular actin networks (24, 25), they have relied on polystyrene beads as scaffolds, which do

Significance

Myosins function as groups of motors anchored to a cellular scaffold that interacts with neighboring actin filaments patterned in complex three-dimensional networks. Although much is known about the function of individual myosin molecules, the contribution of intermotor interactions to collective movement is poorly understood. We used a precisely engineered biomimetic system to investigate how the mechanics of a structural element in the individual myosin influences the collective motion of groups of motors. Stochastic simulations suggest that the interplay between intramolecular strain on the motor lever arm and intermotor tension dictates trajectory shapes in groups of identical and antagonistic motors. Our study provides a general approach to dissecting emergence in cellular processes with applications for the efficient synthetic design of molecular transport systems.

Author contributions: R.F.H. and S.S. designed research; R.F.H., M.C., and S.S. performed research; R.F.H. and S.S. contributed new reagents/analytic tools; R.F.H. and S.S. analyzed data; and R.F.H. and S.S. wrote the paper.

The authors declare no conflict of interest.

This article is a PNAS Direct Submission.

[1]To whom correspondence should be addressed. E-mail: sivaraj@umich.edu.

This article contains supporting information online at www.pnas.org/lookup/suppl/doi:10.1073/pnas.1315923111/-/DCSupplemental.

not provide control over the number, type, and organization of myosins (24, 25). Here, we use 2D DNA origami scaffolds (26–28) to precisely pattern a combination of myosin V and VI and systematically dissect the role of intermotor interactions on collective function.

In this study, we report the emergence of collective motion in myosins that is dependent on the myosin lever arm. DNA origami scaffolds were used to precisely engineer groups of myosin V and VI motors and study their interactions with a model 2D cellular actin network. A simple model suggests that tuning the flexural rigidity of the lever arm relative to the stiffness of intermotor linkages is sufficient to influence collective trajectories in groups of both identical and antagonistic motors. Our findings suggest that structural features unique to myosin V and VI confer selective advantages to their cellular functions.

Results

Single Myosin V and Myosin VI Move Processively on the Dense Keratocyte Actin Network with Similar Meandering Trajectories. The movement of individual myosin V or VI on dense actin networks (*SI Appendix*, Fig. S1) was first assessed at the single-molecule level with total internal reflection fluorescence (TIRF) microscopy. Myosin V (Fig. 1*A*) moved toward the cell periphery, whereas myosin VI (Fig. 1*B*) traveled toward the cell center, consistent with previously reported actin network polarity (25). The mean speed ⟨v⟩ and mean run length ⟨RL⟩ of a single myosin V (212 ± 10 nm/s; 495 ± 63 nm) or myosin VI (168 ± 2 nm/s; 388 ± 31 nm) are in agreement with previous reports for movement of these myosins on single actin filaments (15, 29, 30). To visually compare the shapes of myosin trajectories, each trajectory was rotated to align their local actin polarity field vectors (Fig. 1*C*; *SI Appendix*, Fig. S2), followed by translation to match starting coordinates. The local actin polarity field vector is the shortest vector that passes through the center of mass of the trajectory, connects the inner and outer boundaries of the keratocyte actin network, and is directed from the cell center to the cell periphery (Fig. 1*C*; *SI Appendix*, Fig. S2). The aligned trajectories show a broad distribution of trajectory shapes for both myosin V and VI (Fig. 1 *D* and *E*). The mean trajectory shape was quantified using the root mean squared displacement of the population relative to the local actin polarity field vector (Fig. 1 *F* and *G*). The mean trajectory shape was also used to quantify the lateral skewness of the trajectories in terms of a shape factor (*S*; *SI Appendix*, Fig. S2), which quantifies the mean lateral deviation (μm) of a population of trajectories as the myosin moves a distance of 1 μm toward the cell center or periphery. Trajectories of single myosin V and single myosin VI had comparable shape factors (0.55 ± 0.3 μm/μm and 0.46 ± 0.3 μm/μm, respectively) that were statistically indistinguishable ($P = 0.11$), suggesting similar meandering movement for both myosin types.

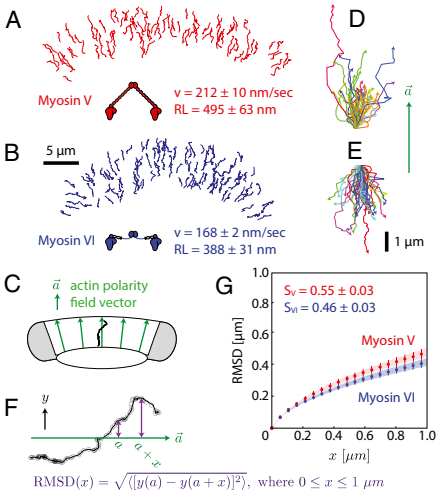

Fig. 1. Single myosin V and VI exhibit similar meandering trajectories. Trajectories of single myosin V (*A*) or myosin VI (*B*) on the keratocyte actin network, colored by direction of movement (red, toward cell periphery; blue, toward cell center). (*C*) The actin polarity field vector (green; *SI Appendix*, Fig. S2) is determined by the shortest distance between the cell center and periphery at any location. The vector points toward the cell periphery. The trajectories on the edges of the keratocyte (gray shaded regions) were excluded from further analysis. (*D* and *E*) Trajectories of single myosin V (*D*) or myosin VI (*E*) aligned with respect to their local actin polarity field vectors. (*F*) Root mean squared displacement calculation of a representative aligned trajectory (black; *SI Appendix*, Fig. S2). (*G*) Root mean squared displacement plots for the aligned trajectories of myosin V (red; $n = 168$) and VI (blue; $n = 203$). The shape factors of single myosin V and myosin VI are statistically indistinguishable ($P = 0.11$), with uncertainties (± SEM) estimated by bootstrapping (*SI Materials and Methods*).

Engineering 2D Actin–Myosin Interactions. To systematically dissect the collective motion of multiple myosin motors, we designed a programmable biomimetic scaffold using a ∼100 nm × ∼80 nm flat rectangular DNA origami (27, 28). The myosin pattern on the origami surface models the interaction at the interface between a myosin-coated vesicle and the cortical actin meshwork that enmeshes it (Fig. 2*A*). Myosin was arranged in a hexagonal configuration, with the side length comparable to the myosin hydrodynamic diameter (Fig. 2 *A* and *B*; *SI Appendix*, Figs. S3 and S4; details in *SI Notes S1*). Myosin V and VI dimers were engineered with a SNAP-tag (alkyl-guanine-transferase) to facilitate the covalent attachment of an oligonucleotide. The myosin-linked oligo is complementary to a scaffold extension (Fig. 2*B*). The high efficiency of myosin labeling with oligo (>95%; Fig. 2*C*) was confirmed by a gel-shift assay. Origami scaffolds were designed with a biotinylated strand to facilitate removal of excess myosin (see *Materials and Methods*; *SI Appendix*, Fig. S5) while preserving the origami shape and myosin attachment (*SI Appendix*, Fig. S6). Precise control of myosin number on each scaffold was evident in defined gel-shifts of the origami scaffold in 1% agarose 0.1% SDS gels (94 ± 1% occupancy; Fig. 2*D*; *SI Appendix*, Fig. S6) and a photon counting assay (>92% occupancy; Fig. 2 *E*–*G*). Intact 2D actin networks with net polarity and large surface area were obtained from detergent extracted keratocytes, as previously reported (25) (Fig. 2*H*; *SI Appendix*, Fig. S1). The origami scaffolds move predominately on the surface of the actin network, whose ∼30-nm mean pore size (25) is significantly smaller than the origami scaffold but is comparable to the ∼36-nm step size of myosin V (29) and VI (30) (Fig. 2*I*).

Multimyosin Scaffolds Move Farther at Lower Speeds. The mean speed of scaffolds with 2–6 myosin V or myosin VI motors is significantly lower than that of a single myosin V or VI, respectively (Fig. 3*A*; *SI Appendix*, Fig. S8). This observation is similar to previous reports for 2 myosin V motors on a single actin filament (15) but is in contrast to kinesin molecules that show essentially no change in speed with increasing motor number (26, 31). Multimyosin scaffold speed, however, does not depend on motor number (n = 2–6 myosins; Fig. 3*A*). Origami scaffolds with myosin V or VI show a characteristic increase in mean apparent run-length with increasing motor number (15, 32), consistent with the engagement of each additional motor with the actin networks (Fig. 3*B*; *SI Appendix*, Fig. S9). Given the limited width of the keratocyte actin network (∼5 μm), the myosin-dependent run length is substantially larger (*SI Appendix*, Fig. S10) than the observed run length (Fig. 3*B*). In both analyses, conjugating a DNA scaffold to a single myosin V or VI does not alter its speed ($P \ge 0.07$; Fig. 3*A*) and mean apparent run length ($P \ge 0.09$; Fig. 3*B*).

Emergent Linear Trajectories in Myosin VI Groups. Trajectories of multiple myosin V-driven scaffolds (Fig. 3 *C* and *E*; Movie S1, *Upper*) are qualitatively similar to those of a single myosin V

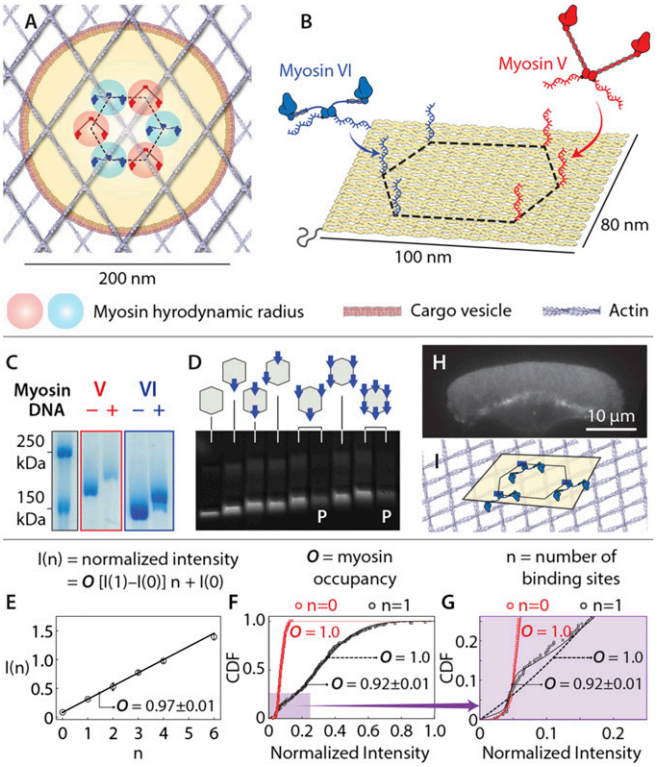

Fig. 2. Scaffolds precisely patterned with myosin V and/or VI. (*A*) Schematic depicting the interaction between a myosin-coated vesicle (yellow) and the cortical actin meshwork. In this model, myosins are closely packed in a hexagonal pattern (dashed hexagon) on the surface of a vesicle. (*B*) Illustration of a flat, rectangular DNA scaffold indicating positions of myosin attachment along the vertices of a hexagon (35-nm side). (*C*) Coomassie staining of SDS/PAGE gel of myosin V and VI before and after conjugation to benzylguanine-DNA. (*D*) SDS-agarose gel showing bands (Cy3 emission) corresponding to scaffold–myosin complexes. Myosin number and pattern are indicated. P, complexes purified by strand displacement (*SI Appendix*, Fig. S5). (*E*–*G*) More than 92% of myosin binding sites are occupied, as assessed with Cy3-labeled oligos. DNA scaffolds were labeled with Cy5, and myosin-binding sites were labeled with complementary Cy3 oligos (*SI Materials and Methods*). (*E*) Normalized intensities (Cy3/Cy5) increase linearly with number of myosin-binding sites, with 97 ± 1% occupancy at each site. (*F* and *G*) Cumulative distribution functions of normalized intensities for scaffolds with 0 ($n = 0$) and 1 ($n = 1$) binding sites. Intensity of scaffolds with no binding sites ($n = 0$) follow a single Gaussian distribution, whereas those with a single binding site ($n = 1$) are consistent with two populations with 92 ± 1% occupancy. (*H*) Representative detergent-extracted keratocyte actin network stabilized with Alexa488-phalloidin (*SI Appendix*, Fig. S1). (*I*) Schematic of scaffold-myosin movement on the surface of the keratocyte actin network. Mesh size of network (~30 nm) (43) is smaller than the size of scaffold (~100 nm). The keratocyte actin network is depicted by actin filaments oriented at ±35° (44). Error bars represent ± SEM.

(Fig. 1 *A* and *D*). In contrast, myosin VI-driven trajectories are highly linear (Fig. 3 *D* and *F*; Movie S1, *Lower*) and are strikingly different from the corresponding single-molecule movement (Fig. 1 *B* and *E*). Correspondingly, the shape factors for myosin VI, but not myosin V, trajectories decrease with increasing motor number (Fig. 3*G*). The similar trajectory shapes for single myosin V or VI molecules (Fig. 1 *A* and *B*) support a role for myosin structure rather than asymmetric organization of the actin network in the observed difference in the collective behavior of groups of motors.

Stochastic Simulation Suggests the Flexibility of the Lever Arm Influences Collective Myosin Movement. To understand the underlying mechanisms that give rise to the difference in movement patterns, a biophysical model was used to study the potential contribution of intra- and intermolecular forces to collective movement. In this model, the stepping process of an individual myosin within an ensemble (Fig. 4*A*; *SI Appendix*, Figs. S11 and S12) is guided by the interplay between the intramolecular strain on the lever arm and the intermolecular tension caused by the stretching of intermotor links (Fig. 4*B*). The flexural rigidity of the lever arm (k_f) imposes an intramolecular penalty for misalignment of the lever relative to the actin filament where the corresponding myosin head is anchored. In contrast, the extension of structural elements in the motors and linkers between them increases the intermotor tension in proportion to the net spring stiffness (k_s; Fig. 4*B*). Therefore, the Boltzmann probability of a given poststroke state derives from the relative magnitudes of the elastic potential energies associated with intramolecular strain and intermotor tension. Stochastic simulations based on this model showed that for an ensemble with defined k_s, trajectory shapes can be tuned by varying k_f/k_s (Fig. 4*C*). Simulated trajectory shapes were quantified in terms of shape factors (Figs. 1*G* and 3*G*; *SI Appendix*, Fig. S2). For myosins with highly flexible lever arms ($k_f L^2 < k_B T$; left shaded region in Fig. 4*D* and *SI Appendix*, Figs. S13 and S14), thermal fluctuations dictate both individual and collective motion. In this regime, the myosin motor freely steps off-axis to relieve intermotor tension, resulting in highly linear trajectories (low shape factor). For rigid levers ($k_f/k_s \gg 1$, right shaded region in Fig. 4*D* and *SI Appendix*, Figs. S13 and S14), the motor steps minimize intramolecular strain. Thus, after release of the trailing head from an actin filament, it preferentially binds to an actin filament with the same spatial orientation as the one bound to the leading head. Subsequent steps by either motor continue to align the heads relative to each other, further minimizing intramolecular strain. The resulting trajectories meander about the local actin polarity field vector with a shape factor that increases with k_f/k_s. The orientation of trajectories for rigid levers ($k_f/k_s \gg 1$)

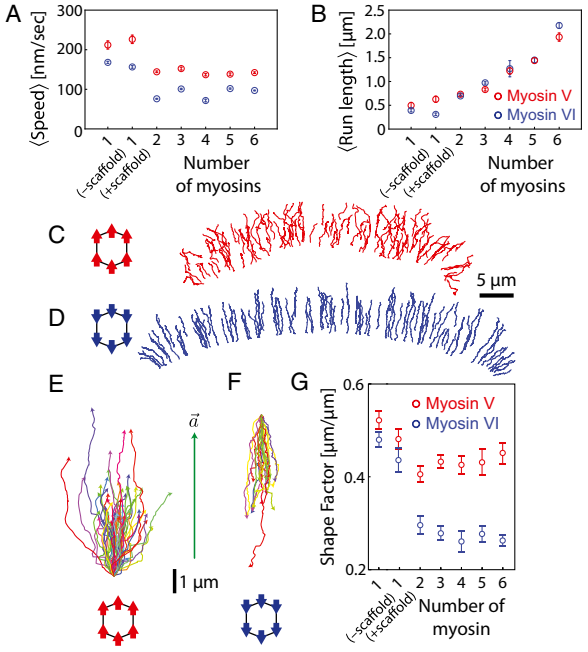

Fig. 3. Collective movement of multimyosin scaffolds. Variation in (*A*) mean end-to-end speed and (*B*) mean run length as a function of myosin number (*SI Appendix*, Figs. S7–S9). (*C* and *D*) Movement trajectories of indicated scaffold–myosin complexes on the keratocyte actin network (Movie S1), with directionality specified by color (red, toward cell periphery; blue, toward cell center). (*E* and *F*) Movement trajectories of scaffolds with 6 myosin V (*E*) or 6 myosin VI (*F*) aligned relative to the local actin polarity field vector. (*G*) Shape factors as a function of myosin number (myosin VI, blue; myosin V, red; n = 58–636). Error bars are ± SEM.

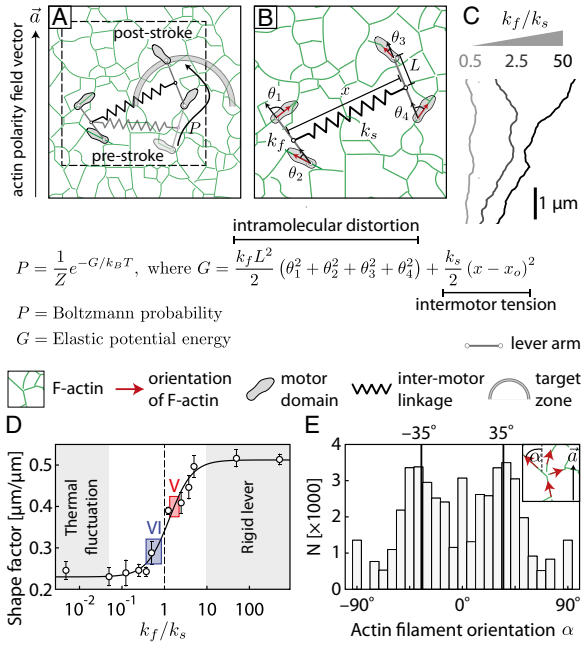

Fig. 4. Model and stochastic simulations of collective myosin movement. (*A*) Simplified model of collective myosin movement on a digitized keratocyte actin network (green; *SI Appendix*, Figs. S11 and S12). The motor domains (gray), lever arms, intermotor linkage (spring), and digitized actin network are drawn approximately to scale. The dashed box corresponds to a zoomed schematic (*B*). The Boltzmann probability of stepping to a target site within the target zone (shaded arc) is a function of the stored potential energy (*G*), which is a function of the net stiffness of the intermotor linkage (k_s) and flexural rigidity of the lever arm (k_f). θ_i is the angle between the lever and the actin filament bound to the motor domain, and x_i is the intermotor distance. (*C*) Representative trajectories generated from the stochastic simulation (*SI Appendix*, Fig. S12) for $k_f/k_s = 0.1$, 0.5, and 50. (*D*) Shape factor as a function of k_f/k_s. Solid line is the least squares fit based on a sigmoidal curve (*SI Appendix*, Figs. S12–S14). Gray shaded regions indicate the two regimes in which the shape factor is not sensitive to k_f/k_s. The experimentally measured shape factors for scaffolds with 2 myosin V (red shaded box) or 2 myosin VI (blue shaded box) yield k_f/k_s values of 1.8 ± 0.35 and 0.50 ± 0.15, respectively. (*E*) Distribution of local actin orientation relative to the actin polarity field vector (α; *Inset*) in the digitized TEM image of keratocyte actin network (*SI Appendix*, Fig. S11). Solid lines corresponds to the characteristic Arp2/3 branch angle of the keratocyte actin networks (±35°), with respect to the actin polarity field vector (44). Error bars represent ± SEM.

depends on the local orientations of actin filaments. Quantitative analysis of transmission electron microscopy (TEM) images of keratocyte actin networks (*SI Appendix*, Fig. S11) yields a bimodal distribution for orientation of actin filaments relative to the local actin polarity field vector, with peaks at ±35° (Fig. 4*E*; *Materials and Methods*). This nonrandom distribution of the underlying actin network contributes to the observed skewed trajectories for $k_f/k_s \gg 1$. Between the extremes dominated by thermal fluctuations and rigid levers, the shape factor steadily increases as (k_f/k_s) increases (Fig. 4*D*, solid line). According to this model, the experimentally observed shape factors are consistent with a flexible lever for myosin VI ($k_f/k_s < 1$) and a relatively rigid lever for myosin V ($k_f/k_s > 1$). For single myosin molecules ($k_s = 0$), the shape factor is solely dependent on the rigidity of the myosin lever relative to thermal fluctuations (k_fL^2/k_BT, where L is the length of the lever arm; *SI Appendix*, Fig. S13). The experimentally observed shape factors for single myosins suggest that both motor types operate outside the regime dominated by thermal fluctuations (*SI Appendix*, Fig. S14).

Swapping Lever Arms Switches Trajectory Shape. Our model demonstrates that the structural properties of the myosin lever arm form a parameter that can account for observed differences in the collective motion of the two myosins. This prediction was tested by experiments involving myosin V and VI chimeras with swapped lever arms. More specifically, chimeras involved the myosin V motor domain with the flexible myosin VI lever arm (myosin V/VI; Fig. 5*A*) and the myosin VI motor domain with the rigid myosin V lever arm (myosin VI/V; Fig. 5*B*). Although the direction of movement is dictated by the motor domain (Fig. 5 *A* and *B*), providing myosin V with a flexible lever arm decreases the shape factors, and vice versa (Fig. 5 *C*–*E*; $n \geq 391$; $P < 0.0001$). This dramatic reversal supports the idea that trajectory shape emerges from the interplay between intermotor tension and lever arm-dependent intramolecular strain.

Trajectory Shape Is Dominated by Myosin V. Myosin V and VI have been shown to colocalize to vesicles in neuronal growth cones (33). Hence, we investigated origami scaffolds with antagonistic motors to test the ability of myosin V and VI to influence each other's movement. In accordance with previous reports, scaffolds with both myosin V and VI commit to one direction of movement (14, 26) and are sorted almost equally into movement toward cell periphery (52 ± 1%) and cell center (48 ± 1%) (Fig. 6*A*; Movie S2; $n = 546$). The shape factor for trajectories with myosin V leading was statistically unchanged compared with those with myosin V alone ($P = 0.37$; Fig. 6*D*). In contrast, the shape factor of trajectories with myosin VI leading was significantly higher than those with myosin VI alone ($P = 0.02$; Fig. 6*D*). This asymmetry suggests that for both inward and outward directed trajectories, the intramolecular strain in the rigid lever arm of myosin V dominates the collective movement, whereas the flexible myosin VI lever follows the path set by myosin V (Fig. 6*E*).

Discussion

Our study illustrates the importance of intermotor interactions in determining collective motion and suggests the need to similarly reconstitute cellular processes to understand the contribution of emergence to higher-order function. Myosin V and VI play important roles in diverse cellular processes, including membrane transport, tethering of organelles, cytokinesis, and actin organization (5). The skewed movement of multimyosin V scaffolds reported here is consistent with the myosin V-driven dispersive motion of pigment granules in the melanocyte cortex (34). In contrast, linear-directed trajectories, rather than meandering motion, are likely to reduce endocytic transport times, as observed in the presence of myosin VI (35). Myosin V and VI move toward

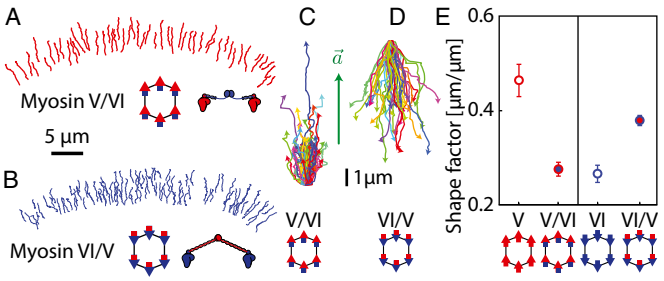

Fig. 5. Exchanging lever arms switches trajectory shapes. (*A* and *B*) Trajectories of scaffolds with indicated myosin chimeras moving along the keratocyte actin network. (*A*) Scaffolds with 6 myosin V/VI (myosin V motor domain with myosin VI lever arm) move toward the cell periphery (red). (*B*) Scaffolds with 6 myosin VI/V (myosin VI motor domain with myosin V lever arm) move toward the cell center (blue). (*C* and *D*) Trajectories of scaffolds with 6 myosin V/VI chimeras (*C*) or 6 myosin VI/V chimeras (*D*) aligned relative to their local actin polarity field vectors. (*E*) Introduction of the myosin VI lever arm decreases the shape factor of the myosin V/VI chimera. In contrast, introduction of the myosin V lever arm increases the shape factor for myosin VI. Error bars represent ± SEM ($n \geq 391$).

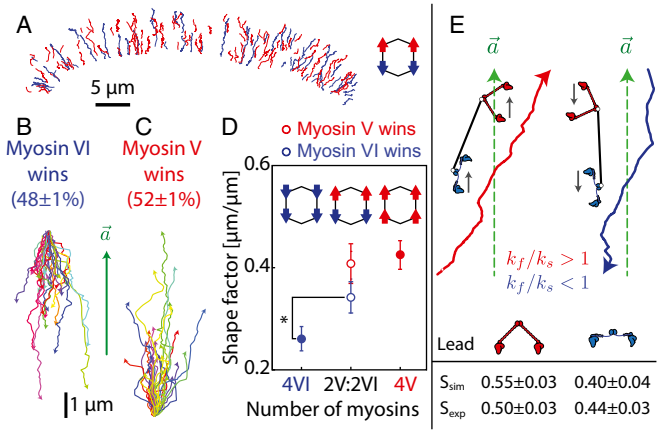

Fig. 6. Trajectory shapes are dominated by myosin V. (*A*) Movement trajectories of scaffolds with 2 myosin V and 2 myosin VI ($n = 546$; Movie S2), with directionality indicated by color (red, toward cell periphery; blue, toward cell center). (*B* and *C*) Percentage of runs to cell periphery (red) and to cell center (blue) is indicated. Trajectories of scaffolds with 2 myosin V and 2 myosin VI moving toward the cell center (*B*) and cell periphery (*C*), aligned relative to the local actin polarity field vector. (*D*) Shape factors for trajectories moving toward the cell periphery (open red circle) or cell center (open blue circle) for scaffolds with 2 myosin V and 2 myosin VI compared with scaffolds with either 4 myosin V or VI. Error bars represent ± SEM. (*E*) Sample simulated trajectories of scaffolds with 1 myosin V ($k_f/k_s = 1.8$) and 1 myosin VI ($k_f/k_s = 0.5$), with either myosin V (left) or myosin VI (right) in the lead ($k_s = 0.2$ pN/nm). The simulated shape factors are significantly higher when myosin V leads ($P < 0.0001$). This asymmetry is also observed in experimental trajectories moving toward the cell periphery or the cell center for matched myosin scaffolds ($n = 425$). Error bars represent ± SEM.

the opposite ends of single actin filaments, albeit with similar stepping kinetics (29, 30). Our study shows that the myosin lever arm can influence trajectory shapes in groups of motors. The structural elements that constitute the myosin lever are unique to each member of the myosin family (36). Myosin V has a relatively rigid lever arm consisting of a series of IQ motifs wrapped by six calmodulin light chains (37). In contrast, myosin VI has only two calmodulin binding domains followed by a semiflexible single ER/K α-helix domain (36). The flexible myosin VI lever is necessary and sufficient to straighten trajectories in groups of myosin VI motors. A parallel observation is that structural elements in myosin X lever arm extension selectively enable processive movement on parallel actin bundles because of the poor processivity of this motor on single actin filaments (17). Accordingly, myosin X preferentially associates and moves along filopodia because of its increased residence time on this actin architecture. Further, single molecules of myosin V, VI, and X display preferential processive movement on distinct actin architecture (13). These observations are consistent with our findings that structural features within the myosin molecule influence cellular behavior by selectively influencing interactions with the actin network. This is in contrast to functional differences in myosins attributed to their distinct cargo binding domains, which are well-established determinants of subcellular localization through the selective binding of membranes or adaptor proteins (38).

Unraveling the rules of interaction between the individuals of a group is an essential step for understanding and controlling emergent behavior (1, 3). Hence, we paired experiments with stochastic simulations that incorporate detailed information on myosin stepping derived from single-molecule studies (37). Such simulations have been previously used to determine the relative population of different kinetic states during the processive movement of two-motor assemblies on single actin filaments (15) or microtubules (20). Our measurements complement a recent report on two-myosin assemblies (15), in that the multimyosin scaffolds move modestly longer distances, at reduced speeds, compared with single myosin molecules. Transition state models have suggested that two-myosin assemblies substantially populate states in which both motors are bound to an actin filament (20). For our multimotor scaffolds, population of states in which multiple motors are bound to an actin filament should decrease the probability that no motor is bound to an actin filament, resulting in longer runs. Correspondingly, we find that scaffold run length linearly increases with myosin number, supporting the concept that each additional motor can interact with actin filaments. The frequent population of states with multiple motors bound to actin filaments is also supported by the trend in speed with increasing motor number. Assuming the motors step asynchronously, we would expect that the stepping kinetics of each myosin are influenced by whether or not the scaffold is anchored to the actin filament by another motor, rather than the number bound. Accordingly, although multimyosin scaffolds move slower than ones with single myosin, their speeds do not depend on motor number.

Given that the trajectory skewness of multimotor assemblies is dependent on the type of lever arm (V or VI), our simulations incorporated the structural differences in the levers in terms of their flexural rigidity. This single parameter is sufficient to capture the observed differences in trajectory shapes for groups of myosin V and VI. The stiffer lever favors binding of myosin heads to actin filaments aligned with each other. Given the nonrandom distribution of local actin orientations, stiffer levers favor skewed orientation of trajectories relative to the actin polarity field vector. Our simplified model suggests that the balance between intermotor tension of the motor linkages and intramolecular strain in the lever arm dictates trajectory shapes. It must be noted that the model substantially simplifies both the actin architecture and computation of intra- and intermolecular interactions and does not account for the potential effects of intermotor forces on stepping kinetics. Hence, although the model can explain the observed behavior, it is entirely possible that additional parameters can similarly influence intermotor interactions to effect similar outcomes. Nonetheless, our findings suggest an elegant design principle for linear transport in a complex, 2D landscape. Regardless of motor type, tuning the balance between intra- and intermolecular interaction energies can control collective movement. This principle can be applied to designing efficient, long-range transport systems at the nanoscale.

Materials and Methods

Myosin Expression and Purification. Recombinant myosin protein was expressed and purified from Sf9 insect cells. Myosin constructs contain an N-terminal FLAG tag, followed by a myosin, leucine zipper (GCN4) to ensure dimerization, alkyl-guanine-transferase (AGT), and His6 tag. Myosin VI consisted of residues 1-992 of *Sus Scrofa* myosin VI; myosin V is constructed from residues 1-1,0099 of *Gallus gallus* myosin V. Both myosin VI and myosin V/VI chimera were cloned into pBiex-1 (Novagen), whereas myosin V and myosin VI/V were cloned into pFastBac dual (coexpresses calmodulin). Protein was expressed by transient transfection (pBiex-1; Escort IV, Sigma) or baculovirus infection of Sf9 cells (Invitrogen). Expressed proteins were affinity purified at 72 h with Anti-FLAG resin (Sigma), using established procedures (39, 40).

Scaffold-Myosin Preparation and Purification. Single-stranded M13mp18 DNA (scaffold strand; N4040S; NEB) were mixed with fourfold excess of short staple strands (unpurified; IDT), followed by 2-h-long annealing, as previously described (27, 28) (*SI Materials and Methods*). Intact scaffolds were separated from excess staple strands, and improperly folded scaffolds by gel purification (0.8% agarose with SyberGreen) and recovered in 30% sucrose, 1× TAE (40 mM Tris, 20 mM acetic acid, 1 mM EDTA), 12.5 mM $MgCl_2$ (41). Purified scaffolds were mixed with an excess of benzyl-guanine-conjugated myosin (*SI Materials and Methods*) and blocking oligos (mixture of 42-nt oligos with randomized sequence) and incubated for 20 min at 37 °C. Scaffold–myosin complexes were separated from excess myosin by affinity purification followed by strand displacement (*SI Appendix*, Fig. S5).

Photon Counting Assay. Fractional occupancy of myosin binding sites on each DNA scaffold were quantified using a photon counting assay. Cy5-labeled DNA scaffolds were incubated with an excess of Cy3-labeled DNA strand for 30 min at 37 °C, followed by 30 min at room temperature. The scaffolds were diluted by a factor of 25,000 in 1× assay buffer (AB) (25 mM KCl, 4 mM $MgCl_2$, 1 mM EGTA, 25 mM Imidazole) + 1 mg/mL BSA, and subsequently immobilized in a neutravidin-coated flow chamber. Unbound Cy3 was removed by extensive washes with 1× AB·BSA. Scaffolds were imaged in 1× AB + [1 mg/mL BSA, 25 μg/mL glucose-oxidase, 45 μg/mL catalase, 1% (wt/vol) glucose] at room temperature, using a TIRF microscope (Olympus IX81; 60× NA 1.48 Apo TIRF objective), a 2× image magnifier (EMCCD iXON Ultra; Andor), a 532-nm laser (Crystalaser CL532-150mW-L), and a 640-nm laser (CUBE 640–100). For each field of view, successive images of Cy3 (excitation at 532 nm) and Cy5 (excitation at 640 nm) emissions were obtained with 2 s exposure time and ∼100-nm penetration depth (Olympus TIRF Illuminator). Cy3 and Cy5 intensities were quantified using custom Mathematica and MATLAB algorithms. Briefly, individual scaffolds were located using a particle tracking algorithm based on Cy5 intensity. Cy3 intensity for each scaffold was normalized by corresponding Cy5 intensity. Cy3 and Cy5 intensities were individually integrated over a 13 × 13-pixel region. Normalized intensity (I) was defined as the ratio between the intensity values in the Cy3 and Cy5 images (Fig. 2 *E*–*G*).

Motility Assays. Keratocytes were derived from scales of *Thorichthys meeki* (Firemouth Cichlids), as previously described (25). Detergent-extracted keratocytes were washed into buffer AB + 1 mg/mL BSA, followed by incubation with myosin-scaffolds in imaging buffer AB + [1 mg/mL BSA, 2 mM ATP, 9.0 μM calmodulin, 1 mM phosphocreatine, 0.1 mg/mL creatine-phosphokinase, 25 μg/mL glucose-oxidase, 45 μg/mL catalase, 1% (wt/vol) glucose, 1 μM blocking oligos] at room temperature. Time-lapse imaging was performed on an epi-fluorescence microscope (*SI Materials and Methods*), with the exception of single-molecule motility assays in Fig. 1. Single-molecule imaging was obtained using a TIRF microscope (*SI Materials and Methods*).

Data Analysis. Trajectories of individual myosin labeled scaffolds were analyzed using custom MATLAB Particle Tracking software (42) and Imaris (Bitplane). A 2D-Gaussian fit was used to estimate scaffold position with subpixel resolution. Intensity of scaffold was used to exclude doublets and aggregates (<10%). The scaffold positions were used to compute run length, end-to-end speed, and local trajectory angle (*SI Materials and Methods*).

ACKNOWLEDGMENTS. The authors thank M. Ritt and T. Tigney for technical assistance. We thank K. Verhey, B. Yurke, A. Dunn, C. Swanson, E. Winfree, A. Gopinath, P. Rothemund, S. Woo, D. Woods, R. Schulman, R. Malik, and R. Sommese for useful discussions and manuscript review. The authors thank E. Winfree and L. Qian for hosting the atomic force microscopy experiments. Research was funded by the American Heart Association Scientist Development Grant (13SDG14270009) and National Institutes of Health Director's New Innovator Award (1DP2CA186752-01). The authors also thank the Single Molecule Analysis in Real-Time Center of the University of Michigan (seeded by National Science Foundation MRI-R2-ID award DBI-0959823).

1. Vicsek T, Zafeiris A (2012) Collective motion. *Phys Rep* 517(3-4):71–140.
2. Helmi A, White SD, de Zeeuw PT, Zhao H (1999) Debris streams in the solar neighbourhood as relicts from the formation of the Milky Way. *Nature* 402(6757):53–55.
3. Moussaïd M, Helbing D, Theraulaz G (2011) How simple rules determine pedestrian behavior and crowd disasters. *Proc Natl Acad Sci USA* 108(17):6884–6888.
4. Lacayo CI, et al. (2007) Emergence of large-scale cell morphology and movement from local actin filament growth dynamics. *PLoS Biol* 5(9):e233.
5. Hartman MA, Finan D, Sivaramakrishnan S, Spudich JA (2011) Principles of unconventional myosin function and targeting. *Annu Rev Cell Dev Biol* 27:133–155.
6. Verkhovsky AB, et al. (2003) Orientational order of the lamellipodial actin network as demonstrated in living motile cells. *Mol Biol Cell* 14(11):4667–4675.
7. Mooseker MS, Tilney LG (1975) Organization of an actin filament-membrane complex. Filament polarity and membrane attachment in the microvilli of intestinal epithelial cells. *J Cell Biol* 67(3):725–743.
8. Al-Khayat HA, Morris EP, Kensler RW, Squire JM (2008) Myosin filament 3D structure in mammalian cardiac muscle. *J Struct Biol* 163(2):117–126.
9. Hooper SL, Hobbs KH, Thuma JB (2008) Invertebrate muscles: Thin and thick filament structure; molecular basis of contraction and its regulation, catch and asynchronous muscle. *Prog Neurobiol* 86(2):72–127.
10. Hasson T, et al. (1997) Unconventional myosins in inner-ear sensory epithelia. *J Cell Biol* 137(6):1287–1307.
11. Sahlender DA, et al. (2005) Optineurin links myosin VI to the Golgi complex and is involved in Golgi organization and exocytosis. *J Cell Biol* 169(2):285–295.
12. Nagy S, et al. (2008) A myosin motor that selects bundled actin for motility. *Proc Natl Acad Sci USA* 105(28):9616–9620.
13. Brawley CM, Rock RS (2009) Unconventional myosin traffic in cells reveals a selective actin cytoskeleton. *Proc Natl Acad Sci USA* 106(24):9685–9690.
14. Ali MY, et al. (2011) Myosin Va and myosin VI coordinate their steps while engaged in an in vitro tug of war during cargo transport. *Proc Natl Acad Sci USA* 108(34): E535–E541.
15. Lu H, et al. (2012) Collective dynamics of elastically coupled myosin V motors. *J Biol Chem* 287(33):27753–27761.
16. Oguchi Y, et al. (2010) Robust processivity of myosin V under off-axis loads. *Nat Chem Biol* 6(4):300–305.
17. Nagy S, Rock RS (2010) Structured post-IQ domain governs selectivity of myosin X for fascin-actin bundles. *J Biol Chem* 285(34):26608–26617.
18. Klumpp S, Lipowsky R (2005) Cooperative cargo transport by several molecular motors. *Proc Natl Acad Sci USA* 102(48):17284–17289.
19. Müller MJ, Klumpp S, Lipowsky R (2008) Tug-of-war as a cooperative mechanism for bidirectional cargo transport by molecular motors. *Proc Natl Acad Sci USA* 105(12): 4609–4614.
20. Driver JW, et al. (2011) Productive cooperation among processive motors depends inversely on their mechanochemical efficiency. *Biophys J* 101(2):386–395.
21. Jamison DK, Driver JW, Rogers AR, Constantinou PE, Diehl MR (2010) Two kinesins transport cargo primarily via the action of one motor: Implications for intracellular transport. *Biophys J* 99(9):2967–2977.
22. Driver JW, et al. (2010) Coupling between motor proteins determines dynamic behaviors of motor protein assemblies. *Phys Chem Chem Phys* 12(35):10398–10405.
23. Jamison DK, Driver JW, Diehl MR (2012) Cooperative responses of multiple kinesins to variable and constant loads. *J Biol Chem* 287(5):3357–3365.
24. Sheetz MP, Spudich JA (1983) Movement of myosin-coated fluorescent beads on actin cables in vitro. *Nature* 303(5912):31–35.
25. Sivaramakrishnan S, Spudich JA (2009) Coupled myosin VI motors facilitate unidirectional movement on an F-actin network. *J Cell Biol* 187(1):53–60.
26. Derr ND, et al. (2012) Tug-of-war in motor protein ensembles revealed with a programmable DNA origami scaffold. *Science* 338(6107):662–665.
27. Rothemund PWK (2006) Folding DNA to create nanoscale shapes and patterns. *Nature* 440(7082):297–302.
28. Woo S, Rothemund PWK (2011) Programmable molecular recognition based on the geometry of DNA nanostructures. *Nat Chem* 3(8):620–627.
29. Mehta AD, et al. (1999) Myosin-V is a processive actin-based motor. *Nature* 400(6744): 590–593.
30. Rock RS, et al. (2001) Myosin VI is a processive motor with a large step size. *Proc Natl Acad Sci USA* 98(24):13655–13659.
31. Furuta K, et al. (2013) Measuring collective transport by defined numbers of processive and nonprocessive kinesin motors. *Proc Natl Acad Sci USA* 110(2):501–506.
32. Schindler TD, Chen L, Lebel P, Nakamura M, Bryant Z (2014) Engineering myosins for long-range transport on actin filaments. *Nat Nanotechnol* 9(1):33–38.
33. Suter DM, Espindola FS, Lin CH, Forscher P, Mooseker MS (2000) Localization of unconventional myosins V and VI in neuronal growth cones. *J Neurobiol* 42(3):370–382.
34. Tuma MC, Gelfand VI (1999) Molecular mechanisms of pigment transport in melanophores. *Pigment Cell Res* 12(5):283–294.
35. Aschenbrenner L, Naccache SN, Hasson T (2004) Uncoated endocytic vesicles require the unconventional myosin, Myo6, for rapid transport through actin barriers. *Mol Biol Cell* 15(5):2253–2263.
36. Spudich JA, Sivaramakrishnan S (2010) Myosin VI: An innovative motor that challenged the swinging lever arm hypothesis. *Nat Rev Mol Cell Biol* 11(2):128–137.
37. Trybus KM (2008) Myosin V from head to tail. *Cell Mol Life Sci* 65(9):1378–1389.
38. Buss F, Kendrick-Jones J (2008) How are the cellular functions of myosin VI regulated within the cell? *Biochem Biophys Res Commun* 369(1-3):165–175.
39. Sweeney HL, et al. (1998) Kinetic tuning of myosin via a flexible loop adjacent to the nucleotide binding pocket. *J Biol Chem* 273(11):6262–6270.
40. Bryant Z, Altman D, Spudich JA (2007) The power stroke of myosin VI and the basis of reverse directionality. *Proc Natl Acad Sci USA* 104(3):772–777.
41. Bellot G, McClintock MA, Lin C, Shih WM (2011) Recovery of intact DNA nanostructures after agarose gel-based separation. *Nat Methods* 8(3):192–194.
42. Churchman LS, Okten Z, Rock RS, Dawson JF, Spudich JA (2005) Single molecule high-resolution colocalization of Cy3 and Cy5 attached to macromolecules measures intramolecular distances through time. *Proc Natl Acad Sci USA* 102(5):1419–1423.
43. Svitkina TM, Verkhovsky AB, Borisy GG (1995) Improved procedures for electron microscopic visualization of the cytoskeleton of cultured cells. *J Struct Biol* 115(3): 290–303.
44. Maly IV, Borisy GG (2001) Self-organization of a propulsive actin network as an evolutionary process. *Proc Natl Acad Sci USA* 98(20):11324–11329.

Supporting Information for

Title: Myosin lever arm directs collective motion on cellular actin network

Author affiliation:

Rizal F. Hariadi[a], Mario Cale[b], and Sivaraj Sivaramakrishnan[a,b,c]
[a]Department of Cell and Developmental Biology,
[b]Department of Biohysics,
[c]Department of Biomedical Engineering,
University of Michigan, Ann Arbor, Michigan 48109, USA

Corresponding author

Sivaraj Sivaramakrishnan
3045 BSRB,
109 Zina Pitcher Place,
Ann Arbor, MI 48109-2200, USA
Ph: 734-764-2493
Fax: 734-763-1166
e-mail: sivaraj@umich.edu

This PDF file includes

Supplemental Methods
Supplemental Figures S1–S14
Legends for Supplemental Movies S1–S2
Supplemental Notes S1
Supplemental Table S1

Supplemental Methods

Buffer and reagents – 1X Assay Buffer (AB) - 25 mM imidazole (pH 7.5), 4 mM $MgCl_2$, 1 mM EGTA, 25 mM KCl, 10 mM DTT; 1X AB.BSA buffer, AB buffer + 1 mg/mL BSA.

Preparation of benzyl-guanine-conjugated oligo – C6-amine modified oligonucleotides (oligo) were covalently linked to benzyl-guanine NHS-ester (BG-GLA-NHS; NEB). Briefly, 0.08 mM oligo was incubated with 3.2 mM BG-GLA-NHS in 0.1M $NaBO_3$ for ~8 hr at room temperature with shaking. Oligo was precipitated in a final concentration of 70% ice-cold ethanol followed by multiple washes and centrifugation (12,000g; 30 min) steps to remove unreacted BG-GLA-NHS. Air-dried pellet was reconstituted in 2 mM Tris pH 8.5 followed by desalting (2x) on G-50 MicroColumns (GE Healthcare). Final benzyl-guanine labeled oligo (BG-oligo) concentration was determined from UV absorbance at 260 nm (Nanodrop). BG oligo aliquots were frozen and stored at -80 °C.

Covalent oligo attachment to myosin protein – Myosin protein bound to Anti-FLAG resin was incubated with excess (>10 μM) of benzyl-guanine-conjugated oligo (BG-oligo) at 37 °C with shaking for 30 min followed by overnight incubation on ice. Resin was washed 3 times with buffer containing 20 mM Imidazole pH 7.4, 3 mM DTT, 1 μg/ml PMSF, 10 μg/ml aprotinin, and 10 μg/ml leupeptin. BG-oligo labeled myosin was eluted with 0.2 mg/ml FLAG-peptide (Sigma) and was used within two weeks or stored in a 55% v/v glycerol solution at –20 °C. Labeling efficiency was assessed by separating labeled and unlabeled myosin by 10% SDS-PAGE followed by staining with SimplyBlue SafeStain (Invitrogen). Myosin labeled with BG-oligo showed a distinct gel-shift with over 95% labeling efficiency quantified by densitometry.

Origami preparation and purification – DNA sequences are listed in the SI Notes 1. Three strands are used in tandem to enable purification of scaffold-myosin complexes by strand displacement (Fig. S5). The origami-attachment strand is an extended staple strand; the spacer strand has complementarity to the origami-attachment strand; the biotin-strand has complementarity to the spacer strand. Further, staple strands at the sites of myosin attachment have a 5T's extension to provide the bound myosin with rotational freedom. Last, the 23 edge- staple strands were extended with a unique DNA sequence. A single Cy3 DNA strand with complementarity to this edge-staple extension was used to label each scaffold with 23 Cy3 dye molecules. Purified scaffolds were stored at 4 °C.

Scaffold-myosin purification – Affinity purification was achieved with a nitrocellulose coverslip coated with neutravidin. Biotinylated, myosin-scaffold mixtures were bound to the coverslip for 5 min. Subsequently, the coverslips were extensively washed with AB supplemented with 0.1 mg/ml BSA. Myosin scaffolds were eluted with AB.BSA and 9 μM calmodulin. Elution was achieved by competitive displacement of the spacer strand with a highly complementary elution strand (10 min at RT; Fig. S5). Purified myosin-scaffold complexes were immediately used in motility assays. The yield and integrity of scaffold- myosin conjugation was assessed using 1% agarose - 0.1% SDS gels.

SDS-Agarose Gel – The purity, yield, and structural integrity of myosin-origami conjugation was assessed by a gel-shift assay. The myosin-origami samples were incubated with loading dye (Promega) containing 1% SDS for 5 minutes. The samples were loaded onto 1% agarose-0.1% SDS gel and run in 1X TE, 0.1% SDS, and 5 mM $MgCl_2$ for 6-10 hours, at 60 V, at room temperature.

Cy3-myosin conjugation for single molecule experiments – Purified BG-oligo1-labeled myosin dimers were mixed with an excess of Cy3-RC-oligo1-Cy3 strand (5'- Cy3-ACTATAGAGATTGGCGCGTATCGT-Cy3 -3') and incubated in binding buffer (10 mM Imidazole, pH 7.4, 25 mM KCl, 10 mM $MgCl_2$) supplemented with 1 mg/mL BSA and 9 μM calmodulin for 20 minutes at ambient temperature (RC refers to the reverse complement). Cy3-labeled myosin was purified from the excess of Cy3-RColigo1-Cy3 by Nickel-NTA agarose resin (Qiagen). First, the labeled myosin was bound to the resin for 30 minutes on ice. Resin was extensively washed with assay buffer containing 1 mg/mL BSA to remove unbound Cy3-RColigo1-Cy3 strands. The purified Cy3-labeled myosin was eluted from the resin by buffer consisting of 200 mM Imidazole, pH 7.4, 1 mM EGTA, 4 mM $MgCl_2$, 25 mM KCl, 9.0 μM calmodulin, 10 μg/mL Aprotinin, 10 μg/mL Leupeptin, 0.1 mg/mL PMSF, and 10 mM DTT. Potential aggregates were removed by centrifugation for 15 minutes at 21.2×10^3 g on a bench top centrifuge at 4°C.

Preparation of keratocyte actin networks – Keratocytes were derived from scales of *Thorichthys meeki* (Firemouth Cichlids) as previously described (26). All protocols conform to the guidelines of the local animal care and use committee (IACUC). As previously reported (26), keratocytes were detergent-extracted and actin networks were stabilized with phalloidin [50 nM Alexa-488 phalloidin (Invitrogen) with 200 nM unlabeled phalloidin (Sigma)]. Coverslips with detergent extracted keratocytes were stored at 4°C and used in motility experiments within 24 hrs.

Single molecule imaging – Single molecule motility assays were acquired at 240x magnification on an objective-based TIRF microscope (Olympus IX81) with a 60x NA 1.48 Apo TIRF objective (Olympus), 4x image magnifier, EMCCD iXON Ultra, and a 561 nm laser (Coherent, 50 mW max power, 6 mW near objective). Movies of scaffold motility on the keratocyte actin network were obtained at 2 Hz for >20 minutes.

Scaffold-myosin imaging – Motility assays of Cy3-labeled scaffold with myosin motors were imaged at 150x magnification on a Nikon TiE microscope equipped with a 100x 1.4 NA Plan-Apo oil-immersion objective, 1.5x magnifier, a mercury arc lamp, Evolve EM-CCD camera (512 pixel x 512 pixel; Photometrics) and Nikon NIS-Elements software. Movies of myosin-scaffold motility on keratocyte were acquired at 2 Hz for 10–60 minutes per field of view.

Run length and end-to-end speed – Analysis of myosin labeled scaffold movement was restricted to scaffolds that appeared for more than 6 continuous frames (3 sec) and covered a distance of more than 3 pixels (320 nm). Scaffolds that were temporarily stalled were excluded from the run length analysis. Run lengths were measured by fitting a trajectory into linear segments of 300 nm starting with the first appearance of the

scaffold. Run-length distribution was fitted to the truncated cumulative distributive function (CDF) of a single exponential distribution, $CDF(x) = 1\text{-}e^{-(x\text{-}xmin)/\lambda}$, where λ is the mean run length and x_{min} is the *a priori* minimum measurable run length (600 nm). End- to-end speeds were calculated by dividing measured run length (see above) by the total time the scaffold remained bound to the keratocyte network. The run length is reported as mean±SEM of the parameter λ, derived from the fit. The SEM was estimated by the bootstrap method.

Stochastic simulation – Detailed description of the simulation is presented in Fig. S11.

Atomic Force Microscopy imaging – AFM images were acquired using tapping mode on a Nanoscope IIIa (Bruker Corporation). We used a SNL silicon nitride cantilever (Bruker AFM Probes) of length 110 μm and spring constant 0.38 N/m. Samples were imaged in AB with excess myosin and BSA removed by purification with Strepavidin magnetic beads (NEB; S1420S). Briefly, 10 μL of purified sample was deposited on a freshly cleaved piece of mica (Ted Pella), ~ 1 cm × 1 cm in size, affixed to a 15-mm diameter magnetic stainless steel puck (Ted Pella). After the DNA scaffolds are immobilized on the mica, an additional 20 μl of AB was added to both sample and cantilever holder before imaging.

Statistical analysis –The p values were computed by two-tail unpaired Student's t test using Prism 6 data analysis software (GraphPad). All reported measurements are expressed as mean ± standard error of mean (SEM). The bootstrap method was used to estimate the uncertainty (SEM) of a measurement of X from the full data set. Bootstrap method was used to analyze shape factor (*S*; Figs. 1, 3, 4, 5, 6), normalized photon intensity (*I*; Fig. 2), speed (*v*; Figs. 3A and S8), run length (*RL*; Figs. 3B and S9). The analysis was performed with either MATLAB or Mathematica. First, from the full data set of sample size *N*, a subset of size $\lfloor N/2 \rceil$ was randomly chosen to compute x_j. The brackets denote rounding off to the nearest integer. In a random subset, an element was never chosen more than once. The value of x_j was generated ≥1000 times. As *j* increases, the distribution of x_j approaches a normal distribution $\langle x_j \rangle \rightarrow X$. Finally, the standard deviation of x_j was used as an estimate of the uncertainty in the measurement of X.

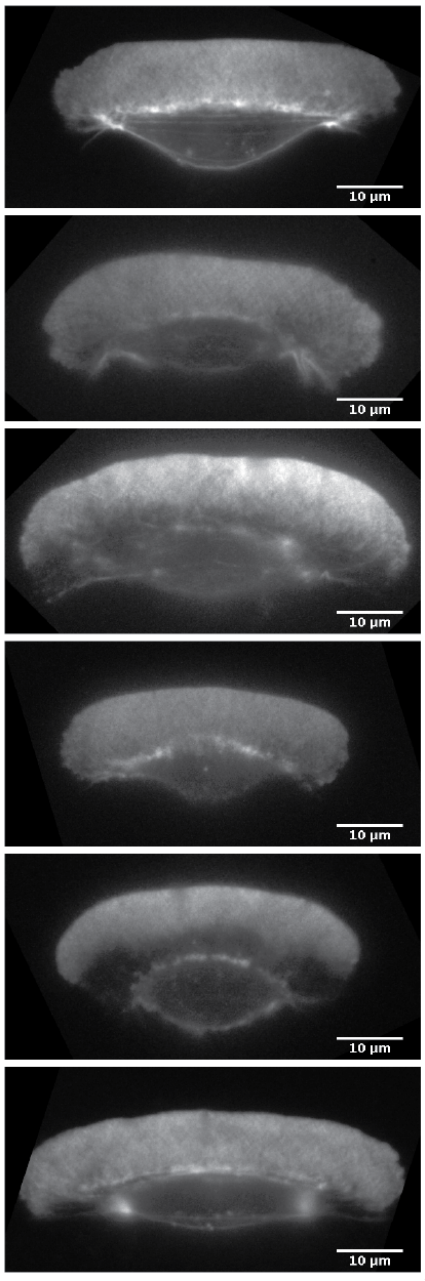

Figure S1 – Sample keratocyte actin networks - Representative fluorescence images of fish epidermal keratocyte networks after detergent extraction. The actin networks were stabilized with a combination of Alexa488-phalloidin and dark-phalloidin (1:4) during the extraction.

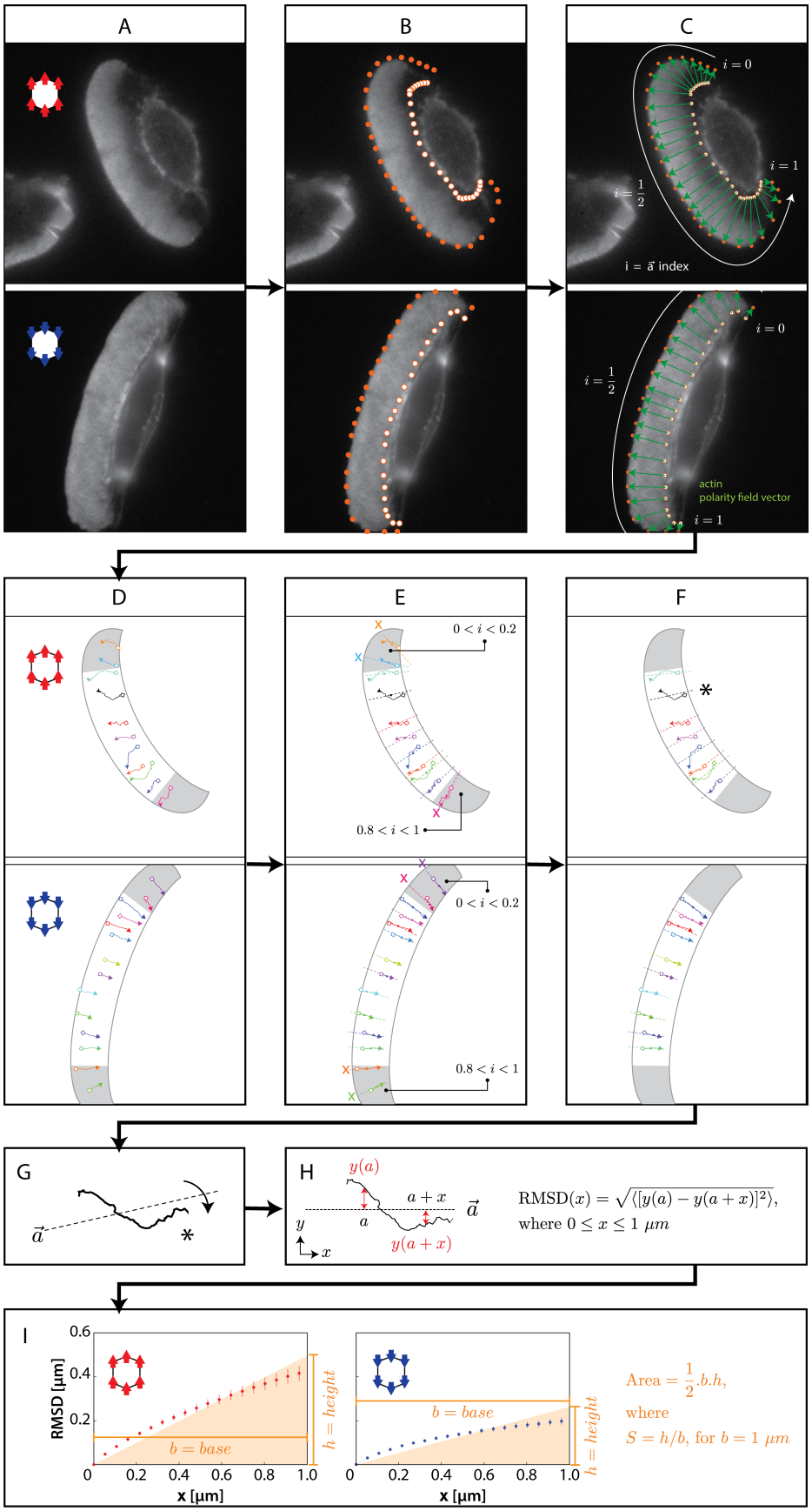
A
B
C
$i = 0$
$i = 1$
$i = \frac{1}{2}$
i = a⃗ index
actin
polarity field vector
D
E
F
$0 < i < 0.2$
$0.8 < i < 1$
G
$\vec{a}$
H
$y(a)$
$a + x$
a
y
x
$y(a + x)$
$\vec{a}$
$\mathrm{RMSD}(x) = \sqrt{\langle [y(a) - y(a+x)]^2 \rangle}$,
where $0 \leq x \leq 1\ \mu m$
I
RMSD [µm]
0.6
0.4
0.2
0
0.2
0.4
0.6
0.8
1.0
x [µm]
$b = base$
$h = height$
$\mathrm{Area} = \frac{1}{2}.b.h,$
where
$S = h/b$, for $b = 1\ \mu m$

Figure S2 (previous page) **– Procedure for calculating the shape factor for a set of trajectories**

(**A**-**F**) Analysis of selected trajectories for scaffolds with either 6 myosin VI (top half) or scaffolds with 6 myosin V (bottom half). These steps were used for computing the shape factor for both experimental and simulated trajectories in Figs. 1, 3, 4, 5, and 6.

(A) Keratocyte image.

(B) Selected coordinates of ≥20 equidistant points near the cell center (open orange circles) and at the cell periphery (closed orange circles).

(C) Vectors connecting points from the cell center to the cell periphery (green arrows) were used to generate a set of actin polarity field vectors across the actin surface. Each vector was given an index $0 \leq i \leq 1$, based on its starting position.

(D) Trajectory coordinates are loaded on to the actin polarity field vector map.

(E) Center of mass $\{x_{CM}, y_{CM}\}$ of each trajectory is calculated as
$x_{CM} = \frac{1}{N}\sum_j^N x_j$ and $y_{CM} = \frac{1}{N}\sum_j^N y_j$
where N is the number of points in a trajectory. A binary search algorithm was used to find an actin polarity field vector (dashed arrows) that passes through $\{x_{CM}, y_{CM}\}$.

(F) Trajectories with index $0 \leq i \leq 0.2$ and $0.8 \leq i \leq 1.0$ were excluded from the data analysis in order to avoid complications due to the possible variation in actin architecture at the keratocyte edges.

(G) The trajectories in (**F**) were rotated to align their local actin polarity field vector to a horizontal axis (x). As an example, the * trajectory in (**F**) was rotated clockwise (**B**). The rotated * trajectory is presented in (**H**).
At this step, aligned trajectories from multiple keratocytes can be combined into a single data set. Examples of ensembles of aligned trajectories are presented in Figs. 1D–E, 3E–F, 5C–D, and 6B–C.

(H) Root mean squared sisplacement (RMSD) was calculated relative to the axis of the local actin polarity field vector ($\vec{a}$). RMSD is defined as
$RMSD(x) = \sqrt{\langle [y(a) - y(a+x)]^2 \rangle}$, where $0 \leq x \leq 1$ μm.

(I) The RMSD(x) was fit to a polynomial of order n (x^n). The area under this curve was calculated by integrating the fitted polynomial from 0–1 μm. The height of a triangle with the same area and a base of 1 μm is defined as the shape factor. Mathematically, the shape factor (S) is expressed as
$A = \frac{1}{2}.b.h$
where A = area of the shaded triangle, b = base, and
h = height. Then, $S = h/b$, for b = 1 μm.

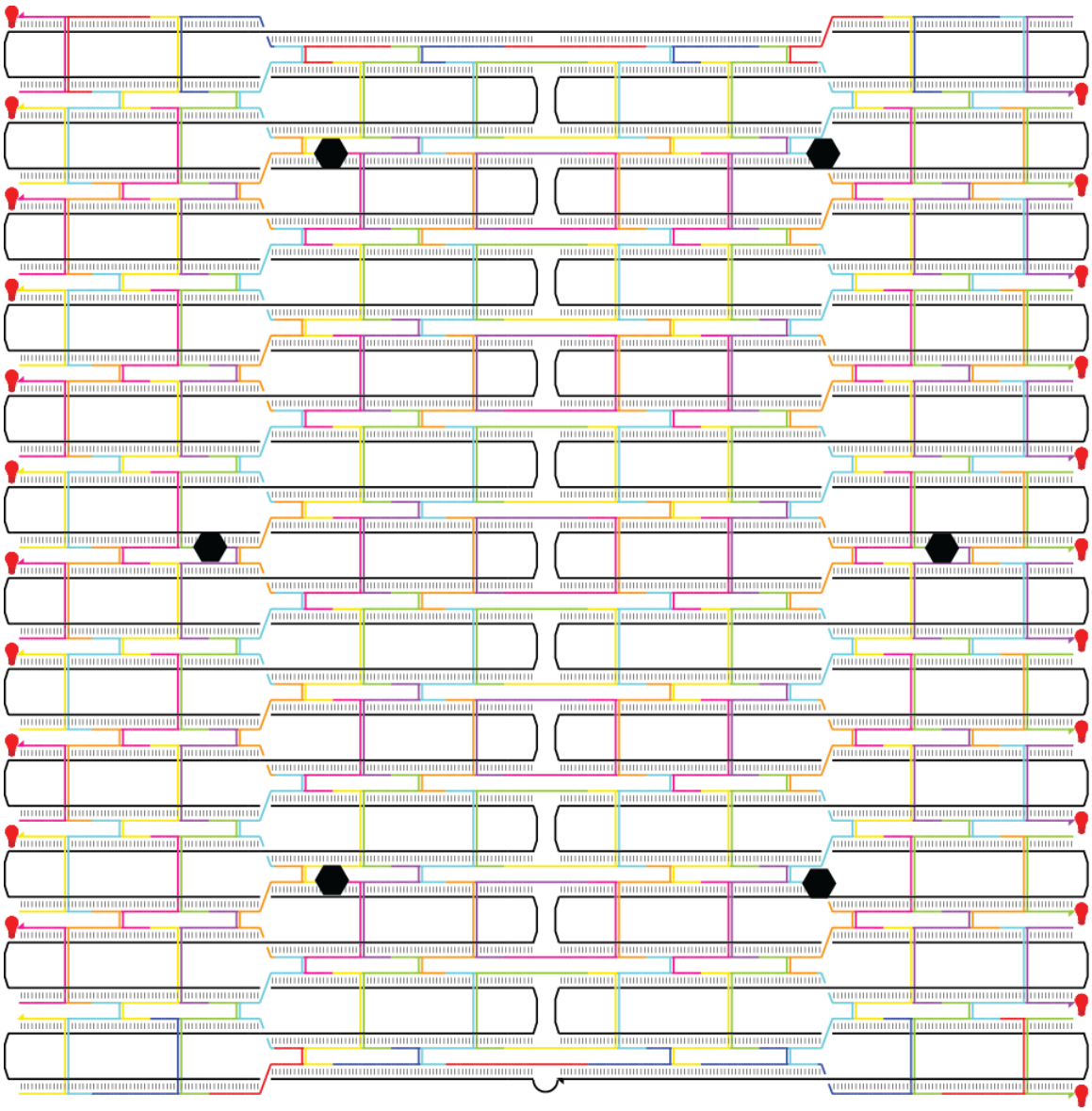

Figure S3 – Flat rectangular DNA origami scaffold design – The main core of the scaffold is a flat rectangular DNA origami with 10.44 bp/turn, consisting of 24 parallel DNA helices *(Woo and Rothemund, Nat. Chem, 2011)*. The scaffold strand is shown as a continuous thick black line. The 6 possible attachment sites for DNA-labeled myosin V or VI are depicted as black hexagons. The bottom left staple strand is extended for affinity-based purification (Fig. S5). With the exception of the edge-staple strand at the bottom left corner, each staple strand is labeled with 23 Cy3 fluorophores (shown as red light bulbs) to facilitate single molecule microscopy and myosin occupancy assays.

Figure S4 - Sequence diagram for a flat rectangular DNA origami scaffold with 10.44 bp/turn *(Woo and Rothemund, Nat. Chem., 2011)* – The scaffold strand is displayed in white.

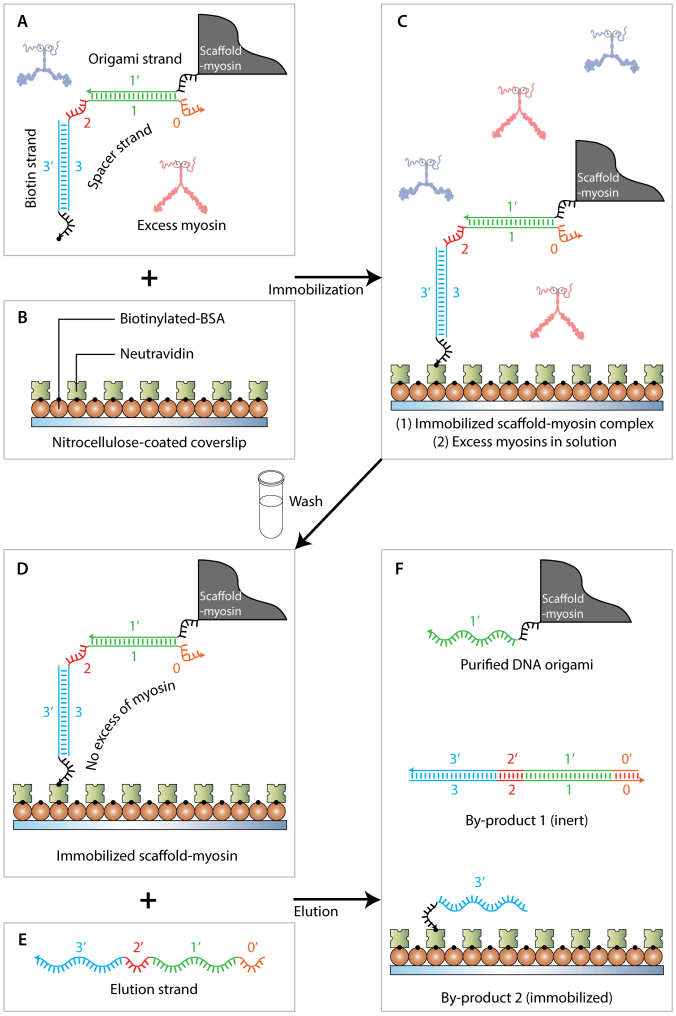

Figure S5 – Purification steps to remove the excess myosin – (**A**) Each scaffold is agarose-purified to remove excess staple strands. The agarose-purified scaffold (gray) contains three short oligos for further purification of scaffold-myosin complexes, namely an origami strand (1'; green), a biotin strand (3'; blue), and a spacer strand (123; green-red-blue). (**B**,**C**) The origami-myosin complexes are immobilized on a neutravidin-coated surface (22x22 mm coverslip) by a BSA-biotin-neutravidin linkage. The unconjugated myosins are free in solution. (**D**) The excess myosin is washed away by a gentle immersion step in a 50 mL Falcon tube filled with AB (see SI Methods) and 0.1 mg/mL BSA. (**E**) An elution strand (0'1'2'3'; orange-green-red-blue) is presented to the immobilized scaffold-myosin complex. (**F**) The elution strand releases the scaffold-myosin complex into solution by a branch migration reaction, while releasing the inert elution-spacer complex as a by-product. Purified myosin-scaffold complexes are immediately used in motility assays.

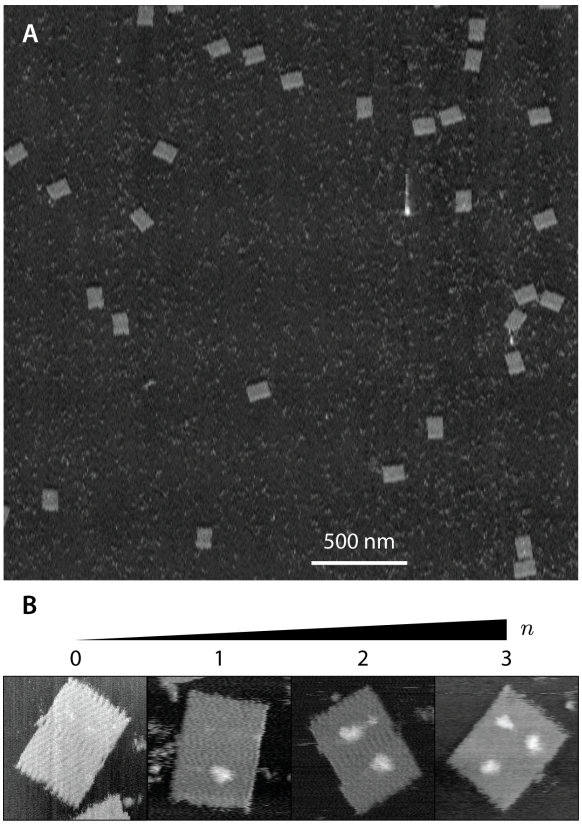

Figure S6 – AFM images of purified DNA scaffolds – (**A**) Representative AFM image of purified DNA scaffolds showing the structural integrity (> 95%) after the purification step (Fig. S5). (**B**) High resolution AFM images of DNA scaffolds with n = 0, 1, 2, and 3 myosin V motors. The size of the DNA scaffold is ~100 nm x 80 nm.

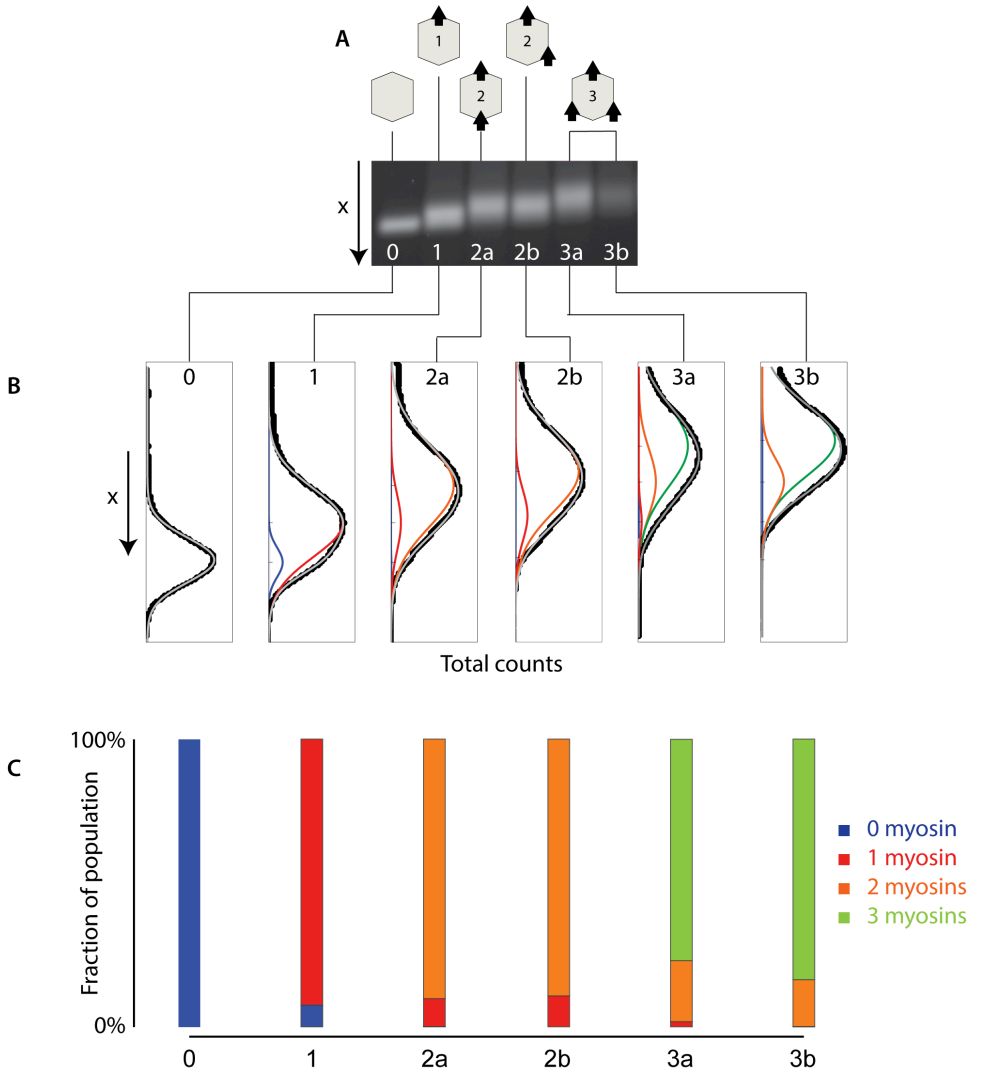

Figure S7 – Quantifying myosin occupancy based on agarose gel shift – (**A**) SDS-agarose gel shift of Cy3-labeled scaffolds with 0, 1, 2, and 3 DNA binding strands in the presence of DNA-myosin complexes. The gel is a duplicate image of Fig. 2D of main text. (**B**) Myosin occupancy was estimated by fitting the intensity profile of each band along the electrophoresis direction (black dots). The intensity profile for each condition is derived from a summation of profiles for distinct myosin occupancies, each of which is assumed to be Gaussian distributed. Thus the intensity profile in each lane is the sum of Gaussians corresponding to 0 (blue), 1 (red), 2 (orange) and, 3 (green) myosins each of which has a distinct mean location along the gel, amplitude, and standard deviation. The observed intensity profiles were iteratively fit to the sum of Gaussians. The fraction of population of scaffolds with *n* myosin was calculated from the area under corresponding Gaussian curve. In our analysis, we assume that each myosin-binding process is an independent event. For each binding site, myosin occupancy (O) is defined as the probability of binding. Global fitting of the different conditions to a binomial distribution yielded a myosin occupancy of 0.94±0.1. (**C**) Calculated stacked histograms of the population distribution for each condition. The analysis was limited to scaffolds with 3 myosins due to the large number of free parameters in the fitting step. The high myosin occupancy is consistent with similar values estimated from the photon counting assays (O = 0.92–0.97; Figs. 2E–G).

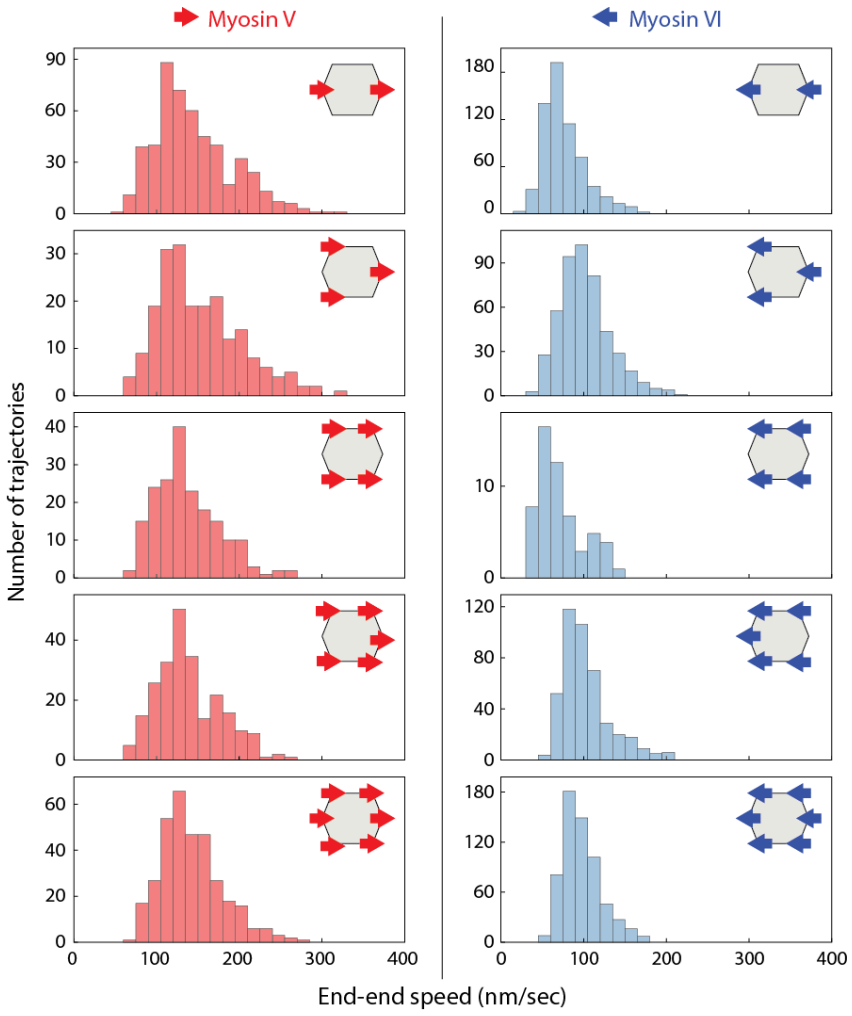

Figure S8 – End-to-end speed distributions for scaffolds with either myosin V or VI – Histograms of end-end speed for the indicated configuration (upper right corner of each histogram) of myosin V (red; left panels) or myosin VI (blue; right panels). Short trajectories (RL<1 μm) are excluded from the data analysis. For either motor type the collective speed does not depend on multi-motor number (P<0.002, $N_V \geq 71$, $N_{VI} \geq 58$). Myosin V scaffolds (regardless of motor number) move significantly faster than those with myosin VI (P <0.01, $N \geq 58$).

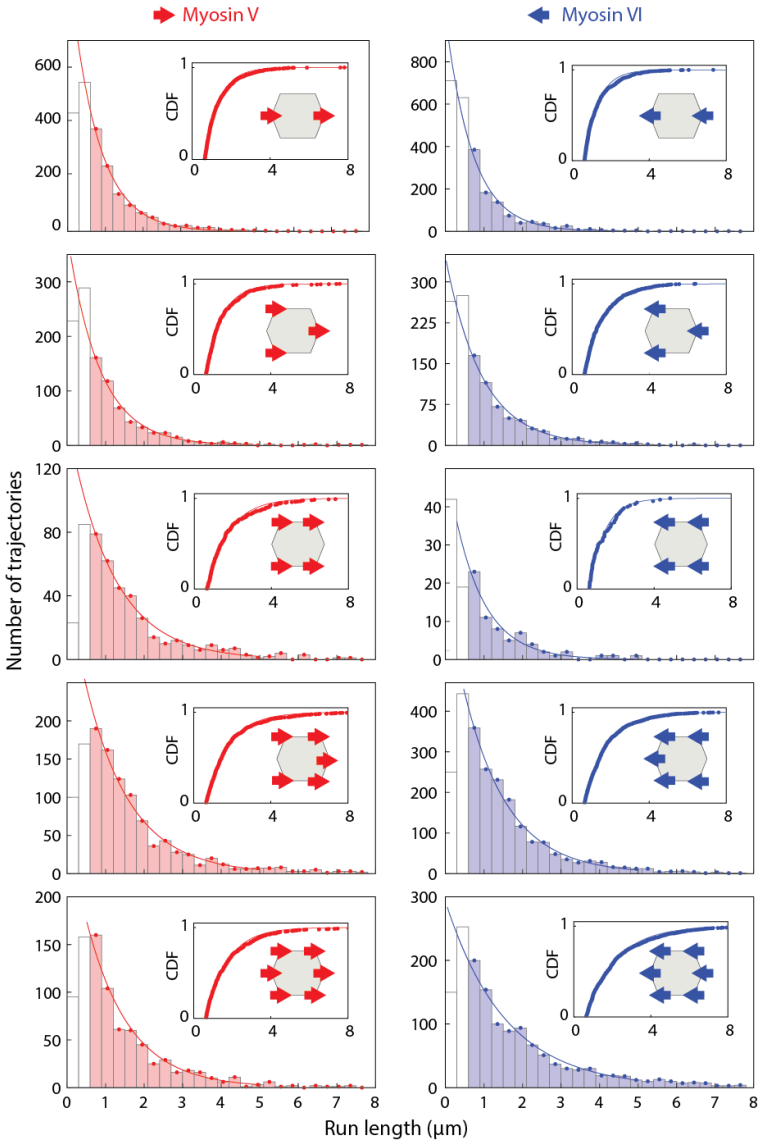

Figure S9 – Run length distribution for scaffolds with multiple myosin V or VI – Run length histograms of scaffolds with myosin V (red; left panels) or myosin VI (blue; right panels). The number and configuration of myosin V (red) and myosin VI (blue) are shown in the insets. Solid lines are single exponential fits based on the cumulative distributive functions (CDF; insets), with a minimum measurable run length (threshold) of 600 nm. The white bars are runs shorter than 600 nm (the number of short runs is an underestimate as they are limited by the spatial and temporal resolution of our image acquisition). For both myosin types, the run length increases with motor number and is summarized in Fig. 3B of the main text.

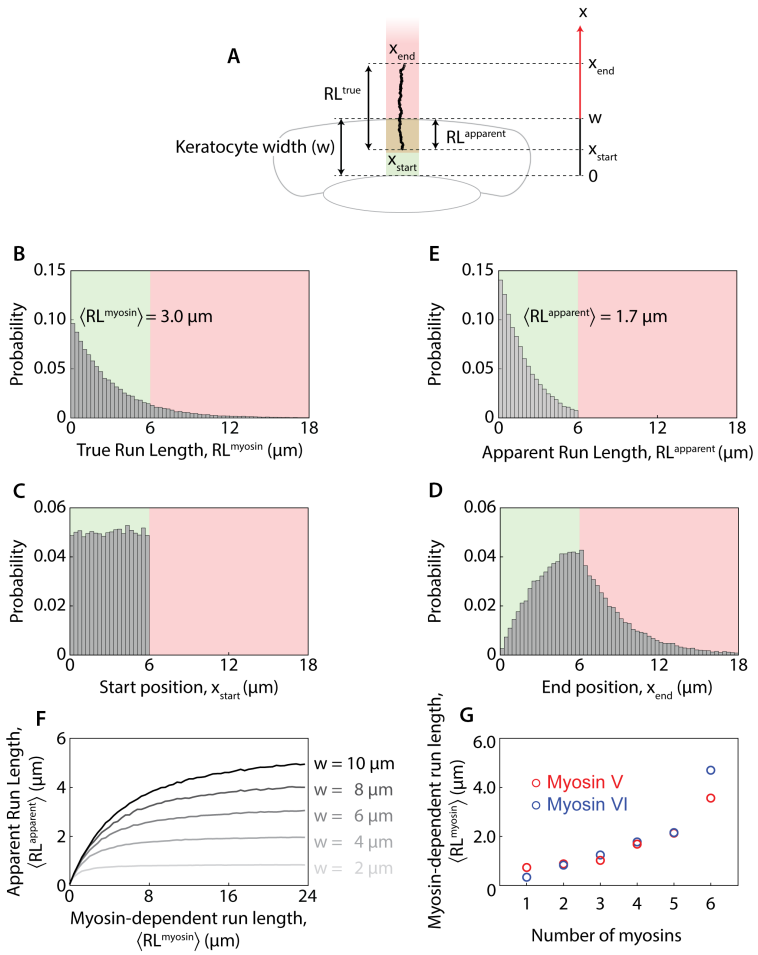

Figure S10 – The measured run length is limited by the finite width of the keratocyte actin network – **(A)** Model for scaffold movement on an infinitely long one-dimensional track. On keratocytes, the track is limited by the keratocyte width w, which is displayed as the green-shaded region in all panels. Scaffolds that enter the red-shaded region are truncated at the keratocyte boundary x=w. **(B)** On an infinitely long track, the distribution of myosin-dependent run lengths (RL_i^{myosin}) follows a single exponential distribution. **(B-E)** The relationship between myosin-dependent and observed (apparent) run lengths is illustrated with w = 6 µm and $\langle RL^{myosin} \rangle$ = 3 µm. **(C)** The start position x_i^{start} of trajectory i is uniformly distributed between 0 and w. **(D)** Trajectory i dissociates from the track at $x_i^{end} = x_i^{start} + RL_i^{myosin}$. Due to the limited keratocyte width, trajectories that travel beyond the keratocyte periphery get truncated at $x = w$. Based on this model, the limited track length preferentially truncates long trajectories. **(E)** As a consequence, the mean apparent run length $\langle RL^{apparent} \rangle$ is calculated to be 1.7 µm, well below $\langle RL^{myosin} \rangle$ = 3.0 µm. **(F)** The mean apparent run length of scaffold-motor complexes with $0<\langle RL^{myosin} \rangle<24$ µm on a keratocyte track of width w = 2, 4, 6, 8, and 10 µm. Based on the model, the limit of mean apparent run length $\langle RL^{apparent} \rangle$ on a keratocyte track of width w is $w/2$. **(G)** Estimated myosin-dependent run lengths for average keratocyte width (w) of 6 µm.

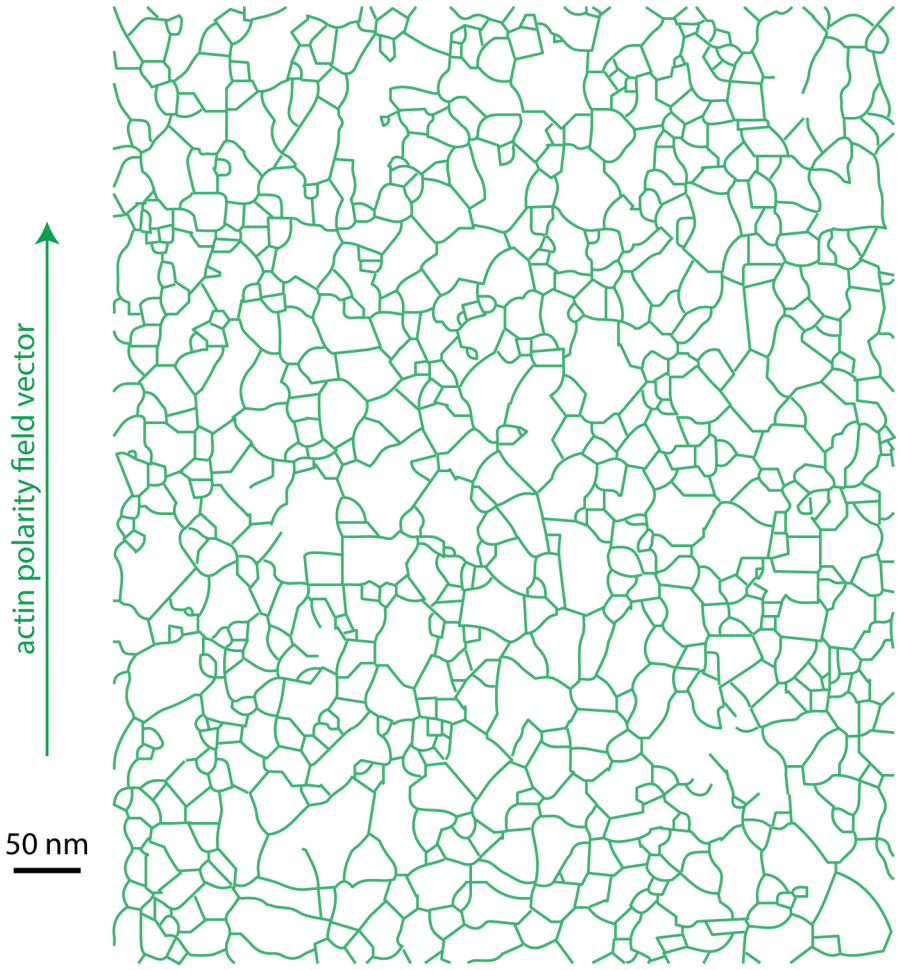

Figure S11 – Skeletonized TEM image of the interlaced actin network used in the stochastic simulation (Fig. S12). The actin polarity field vector (green arrow) points upward. Given that the pore size of the meshwork (~30 nm; *Sivaramakrishnan and Spudich, J. Cell. Biol, 2009*) is substantially smaller than that of the origami scaffold, this analysis is restricted to filaments located near the keratocyte surface with depth information derived from the intensity of the platinum replica micrographs (see Methods).

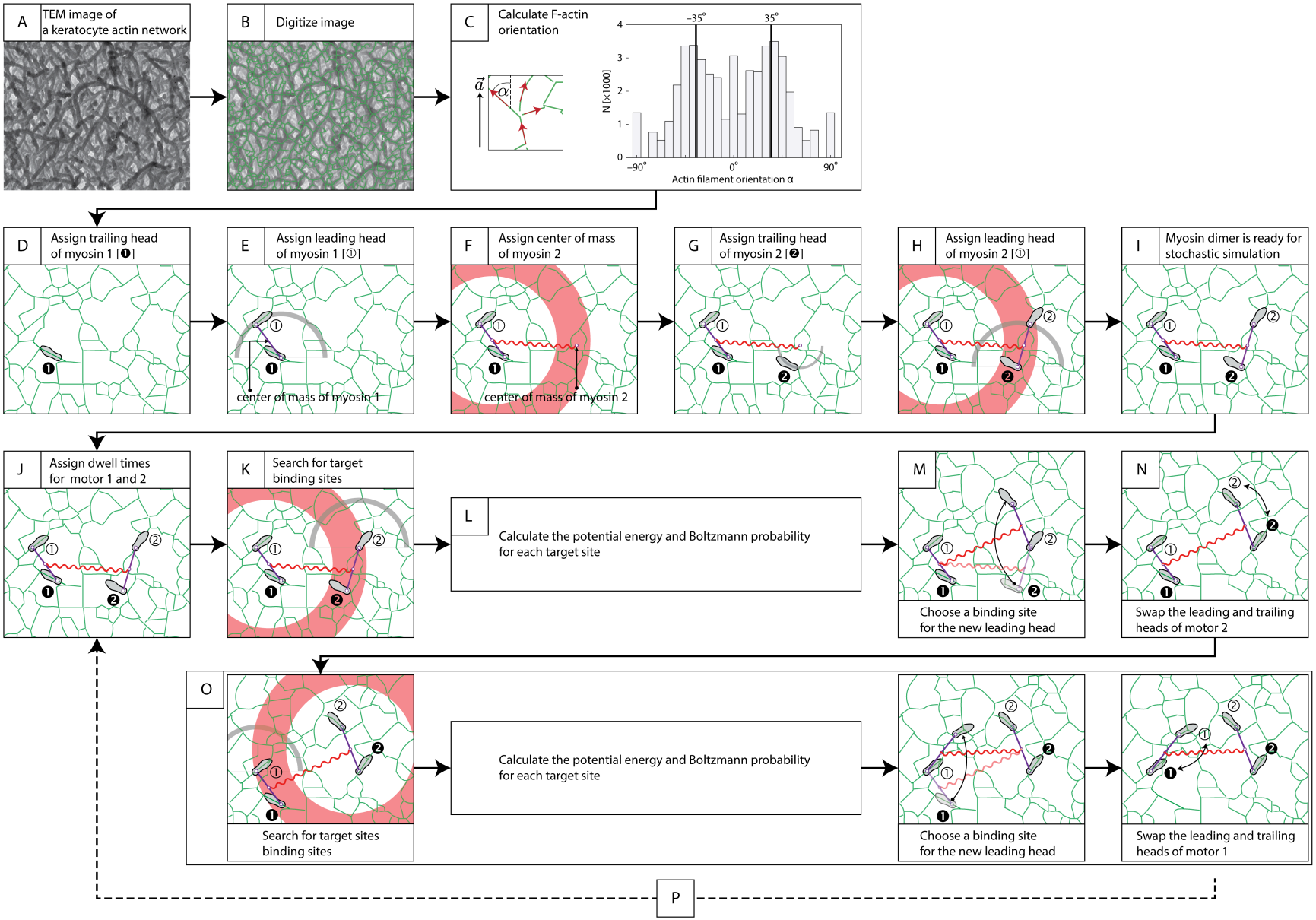
A
TEM image of
a keratocyte actin network
B
Digitize image
C
Calculate F-actin
orientation
$\vec{a}$
α
−35°
35°
N [×1000]
Actin filament orientation α
D
Assign trailing head
of myosin 1 [❶]
E
Assign leading head
of myosin 1 [①]
center of mass of myosin 1
F
Assign center of mass
of myosin 2
center of mass of myosin 2
G
Assign trailing head
of myosin 2 [❷]
H
Assign leading head
of myosin 2 [①]
I
Myosin dimer is ready for
stochastic simulation
J
Assign dwell times
for motor 1 and 2
K
Search for target
binding sites
L
Calculate the potential energy and Boltzmann probability
for each target site
M
Choose a binding site
for the new leading head
N
Swap the leading and trailing
heads of motor 2
O
Search for target sites
binding sites
Calculate the potential energy and Boltzmann probability
for each target site
Choose a binding site
for the new leading head
Swap the leading and trailing
heads of motor 1
P

Figure S12 (previous page) – **Description of stochastic simulation** –

Stochastic simulations of myosin-scaffold movement on the digitized actin network were performed using a custom MATLAB code based on the rules described below.

(A) Platinum replica micrograph image of a keratocyte actin network. This image is used to simulate long movement trajectories using periodic boundary conditions.

(B) The position of actin filaments (green lines) was derived from the digitized image of actin network in (**A**) as described in *Sivaramakrishnan and Spudich, J. Cell. Biol, 2009*. Each pixel is a possible microstate for the myosin head.

(C) For every pixel in the skeletonized image, we calculate the orientation of the actin filament relative to the actin polarity field vector. A 7x7 search box, centered on each actin filament pixel is fitted to a linear function. The local actin filament direction is the inverse tangent (*arctan*) of the slope of the fit line. Actin pixels with low goodness of fits (R^2<0.25, 14% of the detected pixels in (**B**)) were excluded from the simulation in order to exclude multi-filament junctions. The local filament directions are stored in order to calculate microstate energies bed in step (**L**).

In our model, a myosin dimer consists of 2 identical myosins with lever arm stiffness k_f (Fig. 4B) or 2 unique myosins with lever arm stiffness k_{f1} and k_{f2} (Fig. 6E). The centers of mass of myosin 1 and 2 are linked by a linear spring k_s. Each myosin motor comprises 2 motor domains (gray sandals). Each myosin has a leading (① or ②) and trailing head (❶ or ❷).

(D) The trailing head of motor 1 is positioned randomly on an actin filament.

(**E**–**H**) The position of the leading head (**E**) and the second myosin (**F**–**H**) are randomly assigned such that the distance between the heads is 36± 4 nm (gray arc; (**E** and **H**)) and the centers of mass of the two motors are within 65±15 nm (red ring; (**F** and **H**)).

(I) At each simulation step, we keep track the position of 4 myosin heads, 2 centers of mass, and the center of the two centers of mass.

(J) Myosin dimers step stochastically with an exponentially distributed dwell time on the actin filament. Hence, the dwell times for each step are derived from an exponential distribition of mean dwell times based on the cycle rates of myosin V and VI [*De La Cruz et al., PNAS 1999*; *De La Cruz et al, J. Biol. Cell. 2001*]. The myosin with the shortest dwell takes the first step. For illustration purpose, $t_1 > t_2$, and myosin 2 moves first.

(K) The trailing head pivots about the lead head. The next binding site is determined by the following criteria:

a. within 36± 4 nm pixel from the leading head (gray arc),
b. the new center of mass is within 65±15 nm (red ring) from the center of mass of the other motor (myosin 1), and
c. myosins proceed in forward direction based on the polarity of the actin network.

(L) We calculate the energy and Boltzmann probability (Fig. 4B) for each selected pixel.

(M) Based on the Boltzmann probability of each pixel, we stochastically choose the binding site for the new leading head.

(N) The old leading head is now assigned as the new trailing head and the coordinates of the centers of mass are reassigned.

(**O**–**P**) The process is repeated for the other myosin (**J**–**N**) followed by repetitions of (**J**–**O**) to generate trajectories.

For each condition, the simulation was repeated for ≥ 4 times. Simulated trajectory shapes were quantified in terms of shape factor (Fig. S2). To construct the shape factor plots in Figs. 4, S13, and S14, the mean shape factors were fitted to a sigmoidal function (solid lines in Figs. 4 and S14; dashed line in Fig. S13) below:

$S(x) = S_o + a\ \frac{1}{1+e^{-(x-x_o)}}$, where S_o, a, x_o are the fitting parameters and $x = 10^{k_s/k_s}$.

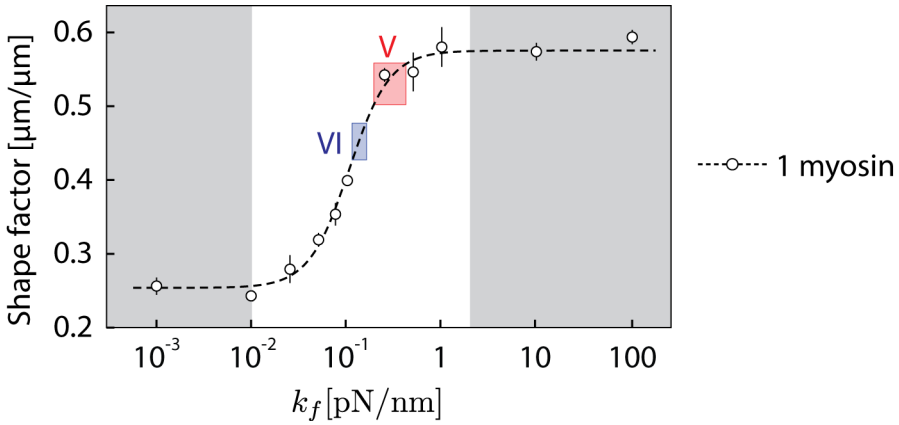

Figure S13 – Lever arm rigidity controls the trajectory shapes for single myosins – Shape factor of simulated trajectories is influenced by the lever arm stiffness k_f. Therefore, the rigidity of the lever arm can be tuned to match the observed trajectory shapes in Fig. 1 of the main text. The experimentally measured shape factors for single myosin V (red-shaded box) or myosin VI (blue-shaded box) were used to calculate corresponding lever rigidities (k_f) of 0.30±0.18 pN/nm and 0.16±0.02 pN/nm, respectively. Movement trajectories of single myosins with either thermally flexible ($k_f L^2 < k_B T$) or rigid ($k_f L^2 >> k_B T$) lever arms are insensitive to k_f (gray-shaded regions).

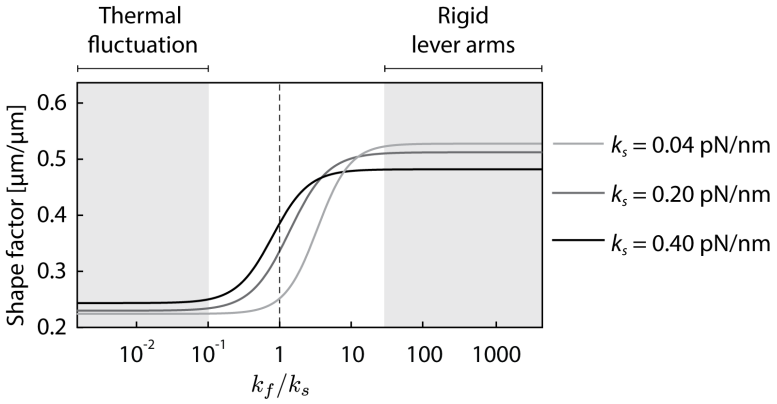

Figure S14 – Shape factors for simulated trajectories of scaffolds with 2 myosin motors connected by an inter-motor spring with stiffness (k_s) = 0.04, 0.20, and 0.40 pN/nm. Sigmoidal lines are derived from simulations with varying k_f / k_s for indicated k_s values. These simulations support k_f / k_s as the primary determinant of trajectory shape factor. Data presented in the main text are for k_s = 0.20 pN/nm. Gray regions indicate regimes dominated by thermal fluctuation or rigid lever arms.

Legends for Movies S1 and S2

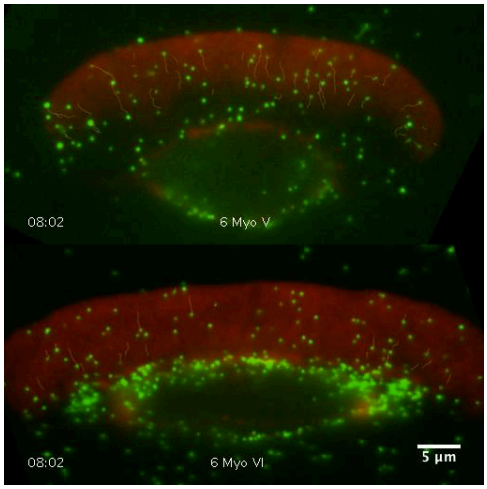

Movie S1 – (**top**) Movie of scaffolds with 6 myosin V (green) meandering on a keratocyte actin network (red) (Fig. 3C). (**bottom**) Scaffolds with 6 myosin VI (green) moving linearly on the two-dimensional network (Fig. 3D). Data was acquired at 2 Hz frame rate, 2 mM ATP, RT.

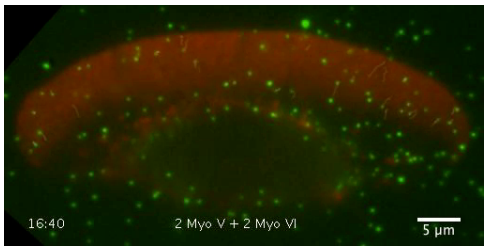

Movie S2 – Scaffolds with 2 myosin V and 2 myosin VI meandering on a keratocyte actin network (red) (Fig. 6A). Scaffolds travel unidirectionally, either towards the cell periphery or the cell center. Data collected at 2 Hz frame rate, 2 mM ATP, RT.

Supplemental Notes S1

Computer aided staple strand sequences for the flat-rectangular DNA origami scaffold (Figs. S3–4)

Core	
r0t11ml1	TTAGATACTATTTTCATTTGGGGAATGCCT
r0t11mr1	TAAGAACGGAGGTTTTGAAGCCTAGTCAGA
r0t11mr2	TAATGCAGTTCGAGCCAGTAATAACTGACCTA
r0t11mr3	AAATCAGAGCTATTTTGCACCCAGAGAATAAC
r0t11mr_fr	ATAAGTCCATATTTAACAACGCCGTGTGAT
r0t11seam_l	AATATCGCTAAGAGGAAGCCCGAAACCTCCCG
r0t11seam_r	CCAGACGACGACAAAAGGTAAAGTATAACCTG
r0t13ml1	GAGTAATGCGGAGACAGTCAAATAACGTTA
r0t13mr1	TAAAGTACCGACAATAAACAACAGGTATTC
r0t13mr2	AATTTAATAAATGCTGATGCAAATTTTTAATG
r0t13mr3	GAGGCATTAACGCGCCTGTTTATCTTCATCGT
r0t13mr_fr	AAATAAGACCTTTTTAACCTCCGTGAGTGA
r0t13seam_l	TTTAGCTAATTTCGCAAATGGTCAAATTCTGT
r0t13seam_r	TATATTTTAGAACGCGAGAAAACTAAAGGGTG
r0t15mr1	CAAGACAAAGTTAATTTCATCTTGAGAATA
r0t15mr3	CTATATGTGGTTTGAAATACCGACCAACATGT
r0t15mr_fr	ATAACCTACAATAACGGATTCGTTATACTT
r0t15seam_l	AGAAAGGCTGTAGGTAAAGATTCATTTTCAAA
r0t17mr3	TCAATTACACATAAATCAATATATGGCTTAGG
r0t19ml1	CCACACAAGGGGTGCCTAATGAGAGCAGGC
r0t19ml3	TCCTGTGTAATTGCGTTGCGCTCAAGAGAGTT
r0t19mr2	CCCTCAATTAACACCGCCTGCAACATTCACCA
r0t19mr_fr	AACAGTTCCACCAGCAGAAGATACATTCTG
r0t19seam_r	AGCATCACGCCAGCAGCAAATGAAATAAAGTG
r0t1ml1	TCCAAAAGTTTCGAGGTGAATTTGTAATGC
r0t1mr2	TTTAACGGGAATGGAAAGCGCAGTCCATCTTT
r0t1seam_r	TTGATGATTCCAGTAAGCGTCATACGGTTTAT
r0t1t_seam	CGCCACCCTCAGAACCGCCACCCTCAGAACCG
r0t1tl1	CCACCCTCAGAGCCACCACCCTCAAAAGGC
r0t1tl2	GGATAGCAAGCCCAATAGGAACCCCAACAGTT
r0t1tl3	TAACACTGAGTTTCGTCACCAGTTTTTCTGT
r0t1tr1	GGTGTATCACCGTACTCAGGAGGTTAATAAGT
r0t21ml1	GAAAATCCCCTTATAAATCAAAACGGCGAA
r0t21ml3	AAGCGGTCGGTTGAGTGTTGTTCCGAGCCCCC
r0t21ml_fl	TTTCCAGTCGTAATCATGGTCACGAAAGGG
r0t21mr2	GTCACACGTTGCAACAGGAAAAACTAAAGGGA
r0t21mr3	GTCAGTATCAATATCTGGTCAGTTGCCCGAAC

r0t21mr_fr	GCCAACATGCTGGTAATATCCAAATCCTGA
r0t21seam_r	AAATGGATTACATTTTGACGCTCACGAAATCG
r0t23b_seam	CGTGGCGAGAAAGGAAGGGAAGAAAATCAGAG
r0t23bl1	GATTTAGAGCTTGACGGGGAAAGCGAATAGCC
r0t23br1	CGGGAGCTAAACAGGAGGCCGATGCTCATG
r0t23br2	TTTTAGACAGGAACGGTACGCCAGGAACAATA
r0t23br3	GAAGTGTTTTTATAATCAGTGAGCTCAAACT
r0t23ml2	CGAGATAGCACGCTGGTTTGCCCCTGAGCTAA
r0t23ml_fl	ACAAGAGCACCGCCTGGCCCTGCTGCCCGC
r0t23mr1	GAAATACCTATTTACATTGGCAGAGTGCCA
r0t23mr3	GCCAGCCAACCAGTAATAAAAGGGAAAACAGA
r0t23seam_l	GCAAAATCTGTTTGATGGTGGTTCATCGTCTG
r0t3ml1	CACTACGAATACACTAAAACACTATCTTGA
r0t3ml2	GCTTGATATTGAAAATCTCCAAAAATTTTCAG
r0t3ml3	GTTTCCATCGATTATACCAAGCGCGACCAGGC
r0t3ml_fl	ACAACCATTGCTAAACAACTTTATGTACCG
r0t3mr1	TTTACCGTACAGGAGTGTACTGGTTAGTAC
r0t3mr2	TCATAATCAATCAAGTTTGCCTTTCAAAAGGG
r0t3mr3	TAAAGCCAGGTCAGTGCCTTGAGTGATATAAG
r0t3mr_fr	ACCGGAATCGATAGCAGCACCGGAAGGTAA
r0t3seam_l	CAGCTTGCGAGCCTTTAATTGTATCATGGCTT
r0t3seam_r	CATAGCCCCGCGTTTTCATCGGCACGAAAGAG
r0t5ml1	CAAGAACCCTGCTCATTCAGTGAAATGCAG
r0t5ml2	ACCCCCAGTAAACGGGTAAAATACCTTAAACA
r0t5ml_fl	GTACAACCTTTGAGGACTAAAGCAATGACA
r0t5mr1	GACTGTAGCCTTATTAGCGTTTGCTCTGAA
r0t5mr2	CGACATTCGAAACGCAAAGACACCATAATAAG
r0t5mr3	AGCGACAGAAAATCACCGGAACCACAAACAAA
r0t5mr_fr	ATATTGAGCAAACGTAGAAAATAGCTATCT
r0t5seam_l	GCAAAAGAAGGCACCAACCTAAAATTTTCGGT
r0t5seam_r	ATATGGTTTTTGTCACAATCAATAAATCAACG
r0t7ml1	ATACATAAAACACTATCATAACCTTGCATC
r0t7mr1	AAGTTTATTACCAGCGCCAAAGAAGCGTCA
r0t7mr2	AGCAAGAATGAACACCCTGAACAATAAATCAA
r0t7mr3	ATATAAAAAACCGATTGAGGGAGGTAATCAGT
r0t7mr_fr	TACCGAAGCAGCCTTTACAGAGCTACAATT
r0t7seam_l	TAACAAAGGGATATTCATTACCCAGAAAATTC
r0t7seam_r	CCACAAGAGAGCGCTAATATCAGAGAGGCATA
r0t9ml1	AAAAAGATGTTTTAATTCGAGCTTTGACCA
r0t9mr1	GGGTAATTATTGAGTTAAGCCCAACGGAAT
r0t9mr2	GATTAGTTTATAGAAGGCTTATCCTGTTCAGC
r0t9mr3	GAATTAACACAATGAAATAGCAATACATACAT

r0t9mr_fr	TTATCCTCAAGCCGTTTTTATTAACAATAG
r0t9seam_l	GTAAGAGCCGCCAAAAGGAATTACGAGATAAC
r0t9seam_r	ACTTGCGGCGAGGCGTTTTAGCGAAGACTTCA
r1t0tr2	GGATAAGTGCCGTCGAGAGGGTTAACAGTGC
r1t0tr3	TAGGATTAGCGGGGTTTTGCTCAGTGCCTATT
r1t10fr1	AGAACAAGGAATCTTACCAACGCTGTCAAAAA
r1t10fr2	TCTTTCCATTAAACCAAGTACCGCATATCCCA
r1t10fr3	AACGGGTAGAGCCTAATTTGCCAAATCCAA
r1t12fr1	AGAATCGCCTGAACAAGAAAAATAACTCATCG
r1t12fr3	TAAAGCCATACGAGCATGTAGAATTCCAAG
r1t14fr1	GAGAGACTGCGTTAAATAAGAATACTTAATTG
r1t14fr2	AATCATAATGAATTTATCAAAATCCGCTATTA
r1t14fr3	GTCAATAGTTACTAGAAAAAGCCACCAGTA
r1t16fr1	CGGGAGAATGCTTCTGTAAATCGTATAGGTCT
r1t16fr2	ATTAATTTATACAGTAACAGTACCCTACCATA
r1t16fr3	AGATGAATTCCCTTAGAATCCTTGAGAAGA
r1t18fr1	CGACAACTATGGAAGGGTTAGAACTTTTACAT
r1t18fr2	TCAAAATTAAGTATTAGACTTTACGGTTATCT
r1t18fr3	GGATTTAGATTTGCACGTAAAACTAACGTC
r1t20fr1	CGAACGAAGAAAGGAATTGAGGAAAAACAATT
r1t20fr2	AAAATATCCTAAAACATCGCCATTGACCTGAA
r1t20fr3	TGATAGCCTTTAGGAGCACTAACCATTTGA
r1t22fr1	ATCGGCCTGAGATAGAACCCTTCTAAAAATAC
r1t22fr2	AGCGTAAGTGCCTGAGTAGAAGAAGCCACCGA
r1t22fr3	ACATCACTAATACGTGGCACAGACGCGAAC
r1t24br4	GTAAAAGAGTCTGTCCATCACGCAGTAATA
r1t2fr1	CAGACGATAACAGTTAATGCCCCCTACCAGGC
r1t2fr2	TCGGAACCCATTGACAGGAGGTTGCGCCACCC
r1t2fr3	GCCGCCAGTATTATTCTGAAACAGAAGGAT
r1t4fr1	TGAAACCACCGCCTCCCTCAGAGCAGGCAGGT
r1t4fr2	TCAGAACCTAGCAAGGCCGGAAACAAGGTGAA
r1t4fr3	ATTACCATGCCACCCTCAGAGCCCAGAGCC
r1t6fr1	GTATGTTACGGAAATTATTCATTAGTCACCAA
r1t6fr2	TTATCACCATGATTAAGACTCCTTGTAAGCAG
r1t6fr3	GAACTGGCGTCACCGACTTGAGCTAGCACC
r1t8fr1	TGAAAATAGCCCTTTTTAAGAAAAATTACGCA
r1t8fr2	ATAGCCGACGATTTTTTGTTTAACAACGAGCG
r1t8fr3	ATAAGAAAACAAAGTTACCAGAACCCAAAA
r-1t0tl4	CAACGCCTGTAGCATTCCACAGATTTGTCG
r-1t10fl1	AAACGAGAGAGTACCTTTAATTGCTACGGTGT
r-1t10fl2	ATAAGAGGCTCAAATGCTTTAAACAGAGGGGG
r-1t10fl3	GAATCCCCTCATTTTTGCGGATGAGCTCAA

r-1t12fl2	GGCAAAGAAAATATGCAACTAAAGTCCTTTTG
r-1t12fl3	CATGTTTTATTAGCAAAATTAAGTTGTACC
r-1t14fl1	GAGAAGCCGAGAGGGTAGCTATTTCATATGTA
r-1t14fl2	TCTACAAATATGACCCTGTAATACACAGGCAA
r-1t14fl3	AAAAACATGGCTATCAGGTCATTTGAACGG
r-1t16fl1	CCCCGGTTGCTTTCATCAACATTACGTAACCG
r-1t16fl2	CGAGTAACAAACTAGCATGTCAATTTGAGAGA
r-1t16fl3	TAATCGTAAACCCGTCGGATTCTGGATAGG
r-1t18fl1	TGCATCTGCTGCAAGGCGATTAAGGGTACCGA
r-1t18fl2	CGCCAGGGGTGTAGATGGGCGCATAATGTGAG
r-1t18fl3	TCACGTTGTTTTCCCAGTCACGAATGCCTG
r-1t20fl1	GCTCGAATTCGGGAAACCTGTCGTACAGCTGA
r-1t20fl2	CATTAATGCTCTAGAGGATCCCCGTTGGGTAA
r-1t20fl3	CAGGTCGAAATCGGCCAACGCGCGTGGTTT
r-1t22fl1	TTGCCCTTTCCACTATTAAAGAACGCCGTAAA
r-1t22fl2	CAACGTCAACCAGTGAGACGGGCAGCCAGCTG
r-1t22fl3	TTCTTTTCAAGGGCGAAAAACCGTCACCCA
r-1t24bl2	GCACTAAATCGGAACCCTAAAGGAGTTTGGA
r-1t24bl3	AATCAAGTTTTTTGGGGTCGAGGTGTGGACTC
r-1t2fl1	ATGGGATTTCGCCCACGCATAACCGCAACGGC
r-1t2fl2	CGGTCGCTGACGTTAGTAAATGAAACAAACTA
r-1t2fl3	TCTTTCCAGAGGCTTGCAGGGAGAGCAGCG
r-1t4fl1	TACAGAGGGGAGATTTGTATCATCACTTTGAA
r-1t4fl2	AATTGTGTCATCGGAACGAGGGTAGATATATT
r-1t4fl3	AAAGACAGCGAAATCCGCGACCTACGGTCA
r-1t6fl1	AGAGGACACTTGAGATGGTTTAATAACGAACT
r-1t6fl2	TAATCATTGGAACCGAACTGACCAGCCTGATA
r-1t6fl3	ATCATAAGGTGAATTACCTTATGGGACGTT
r-1t8fl1	AACGGAACCAAAAGAAGTTTTGCCAGTTCAGA
r-1t8fl2	TAATAGTAAAATCTACGTTAATAATTCAACTT
r-1t8fl3	GGGAAGAAAAATGTTTAGACTGGATTCATT
rt-rem1	AGCACGTATAACGTGCTTTCCTCGTTAG
rt-rem2	ACAGGGCGCGTACTATGGTTGCTTTGACG
rt-rem3	ACCACACCCGCCGCGCTTAATGCGCCGCT
rt-rem4	CAAGTGTAGCGGTCACGCTGCGCGTAACC
rt-rem5	AGCGAAAGGAGCGGGCGCTAGGGCGCTGG

Edge staples that binds to Cy3-labeled oligo3 (complementary sequence to oligo3 in lowercase)

oligo3-TT-Cy3	agctgcaggctcgacctgcgTT/3Cy3Sp/
r1t0_edge_r_2_RC_oligo3	TTTTTTTAGACTCCTCAAGATGAAAGTATTAAGcgcaggtcgagcctgcagct
r1t2_edge_r_2 _RC_oligo3	TTTTTTTCCAGAACCACCACACCACCCTCAGAGcgcaggtcgagcctgcagct
r1t4_edge_r_2 _RC_oligo3	TTTTTTTGCAAAATCACCAGCATTTGGGAATTAcgcaggtcgagcctgcagct

r1t6_edge_r_2 _RC_oligo3	TTTTTTTTAATAACGGAATAGGAAACCGAGGAAcgcaggtcgagcctgcagct
r1t8_edge_r_2 _RC_oligo3	TTTTTTTTATTATTTATCCCGTTACAAAATAAAcgcaggtcgagcctgcagct
r1t10_edge_r_2_RC_oligo3	TTTTTTTTCTTTCCTTATCAACCAATCAATAATcgcaggtcgagcctgcagct
r1t12_edge_r_2_RC_oligo3	TTTTTTTTATACAAATTCTTTGTTTAGTATCATcgcaggtcgagcctgcagct
r1t14_edge_r_2_RC_oligo3	TTTTTTTAGATTAAGACGCTGAAAACATAGCGAcgcaggtcgagcctgcagct
r1t16_edge_r_2_RC_oligo3	TTTTTTTAGATTTTCAGGTTAGAAATAAAGAAAcgcaggtcgagcctgcagct
r1t18_edge_r_2_RC_oligo3	TTTTTTTTCAATAGATAATAAACTAATAGATTAcgcaggtcgagcctgcagct
r1t20_edge_r_2_RC_oligo3	TTTTTTTTTAGTCTTTAATGCAATATTTTTGAAcgcaggtcgagcctgcagct
r1t22_edge_r_2_RC_oligo3	TTTTTTTTACTTCTTTGATTAAATTAACCGTTGcgcaggtcgagcctgcagct
r---1t2_edge_l_2_RC_oligo3	TTTTTTTAACGATCTAAAGTCAGCCCTCATAGTcgcaggtcgagcctgcagct
r---1t4_edge_l_2_RC_oligo3	TTTTTTTGATCGTCACCCTCTTAAAGGCCGCTTcgcaggtcgagcctgcagct
r---1t6_edge_l_2_RC_oligo3	TTTTTTTGAACGAGGCGCAGGCTCCATGTTACTcgcaggtcgagcctgcagct
r---1t8_edge_l_2_RC_oligo3	TTTTTTTATTATACCAGTCACGATTTTAAGAACcgcaggtcgagcctgcagct
r---1t10_edge_l_2_RC_oligo3	TTTTTTTAATCGTCATAAATATAGCGTCCAATAcgcaggtcgagcctgcagct
r---1t12_edge_l_2_RC_oligo3	TTTTTTTAATATAATGCTGTGCTTAGAGCTTAAcgcaggtcgagcctgcagct
r---1t14_edge_l_2_RC_oligo3	TTTTTTTAAAGCTAAATCGGCAATAAAGCCTCA cgcaggtcgagcctgcagct
r---1t16_edge_l_2_RC_oligo3	TTTTTTTACAAGAGAATCGAGCCTGAGAGTCTGcgcaggtcgagcctgcagct
r---1t18_edge_l_2_RC_oligo3	TTTTTTTATTGACCGTAATGCCGTGGGAACAAAcgcaggtcgagcctgcagct
r---1t20_edge_l_2_RC_oligo3	TTTTTTTGTGCCAAGCTTGCCGTTGTAAAACGAcgcaggtcgagcctgcagct
r---1t22_edge_l_2_RC_oligo3	TTTTTTTATTGGGCGCCAGGGGGGAGAGGCGGTcgcaggtcgagcctgcagct
r---1t24_edge_l_2_RC_oligo3	TTTTTTTACTACGTGAACCATCTATCAGGGCGAcgcaggtcgagcctgcagct

Core staples that bind to oligo1-myosin VI

BG-oligo1	TTTTTTgatacgcgccaatctctata
r0t1mr_fr-TR-oligo1	CCGTATATGGCCTTGATATTCAGAGCCACCtatagagattggcgcgtatc
r1t12fr2-MR-oligo1	tatagagattggcgcgtatcTCCTAATTACGCTCAACAGTAGGGAACACCGG
r0t17mr_fr-BR-oligo1	CTGAATACGTATTAAATCCTTTGGCAAATCtatagagattggcgcgtatc
r0t17ml3_hp_org-BL-oligo1	CAGCTTTCCTATTACGCCAGCTGGTAGCTGTTtatagagattggcgcgtatc
r-1t12fl1-ML-oligo1	tatagagattggcgcgtatcCTGGAAGTACATCCAATAAATCATTTTTGCGG
r0t1ml3-TL-oligo1	TTTTCACGCCGATAGTTGCGCCGAACTTTTTCtatagagattggcgcgtatc

Core staples that bind to oligo2-myosin V

BG-oligo2	TTTTTTatgaacttgcgctcaattcc
r0t1mr_fr-TR-oligo1	CCGTATATGGCCTTGATATTCAGAGCCACCggaattgagcgcaagttcat
r1t12fr2-MR-oligo1	ggaattgagcgcaagttcatTCCTAATTACGCTCAACAGTAGGGAACACCGG
r0t17mr_fr-BR-oligo1	CTGAATACGTATTAAATCCTTTGGCAAATCggaattgagcgcaagttcat
r0t17ml3_hp_org-BL-oligo1	CAGCTTTCCTATTACGCCAGCTGGTAGCTGTTggaattgagcgcaagttcat
r-1t12fl1-ML-oligo1	ggaattgagcgcaagttcatCTGGAAGTACATCCAATAAATCATTTTTGCGG
r0t1ml3-TL-oligo1	TTTTCACGCCGATAGTTGCGCCGAACTTTTTCggaattgagcgcaagttcat

Core staples that does not to either oligo 1 nor oligo2 (control)

r0t1mr_fr-TR	CCGTATATGGCCTTGATATTCAGAGCCACC
r1t12fr2-MR	TCCTAATTACGCTCAACAGTAGGGAACACCGG
r0t17mr_fr-BR	CTGAATACGTATTAAATCCTTTGGCAAATC
r0t17ml3_hp_org-BL	CAGCTTTCCTATTACGCCAGCTGGTAGCTGTT
r-1t12fl1-ML	CTGGAAGTACATCCAATAAATCATTTTTGCGG
r0t1ml3-TL	TTTTCACGCCGATAGTTGCGCCGAACTTTTTC

Purification strands

spacer-strand	CGATGGATGACTGACTGATGGATGACTTAAATTGACTATGACTATGATACTGACTGATTACG
biotin-strand	CATCCATCAGTCAGTCATCCATCGTTTTTTT-biotin
origami-strand (r1t0)	TTTTTTTAGACTCCTCAAGATGAAAGTATTAAGTTGGATAGTCAGTATCATAGTCATAGTCAA
elution-strand	CGTAATCAGTCAGTATCATAGTCATAGTCAATTTAAGTCATCCATCAGTCAGTCATCCATCG

Strands for gliding assay

Biotin-Oligo1-C1	biotin-TTTTTTtatagagattggcgcgtatc
Biotin-Oligo1-C1	biotin-TTTTTTggaattgagcgcaagttcat

Supplemental Table S1 – Statistics

Numbers of trajectories analyzed for indicated experimental conditions. Experimental data were collected on at least four different keratocytes. The minimum number of detected trajectories was 112 and on average 852. End-to-end speed and shape factor analyses were restricted to long trajectories (RL ≥ 1 μm; N ≥ 58).

Experiments	**N** (trajectories)	
	All trajectories	Long trajectories; RL≥ 1.000 μm
Myosin V (– scaffold)	791	168
Myosin VI (– scaffold)	1181	203
DNA scaffold + 1 myosin V	413	71
DNA scaffold + 2 myosin V	1688	501
DNA scaffold + 3 myosin V	895	208
DNA scaffold + 4 myosin V	385	191
DNA scaffold + 5 myosin V	776	240
DNA scaffold + 6 myosin V	1398	338
DNA scaffold + 1 myosin VI	317	64
DNA scaffold + 2 myosin VI	1897	636
DNA scaffold + 3 myosin VI	205	86
DNA scaffold + 4 myosin VI	112	58
DNA scaffold + 5 myosin VI	687	437

DNA scaffold + 6 myosin VI	1185	617
DNA scaffold + 6 myosin V/VI	452	391
DNA scaffold + 6 myosin VI/V	569	492
DNA scaffold + 1 myosin V + 1 myosin VI	828	425
DNA scaffold + 2 myosin V + 2 myosin VI	1837	546

Supporting Information

Hariadi et al. 10.1073/pnas.1315923111

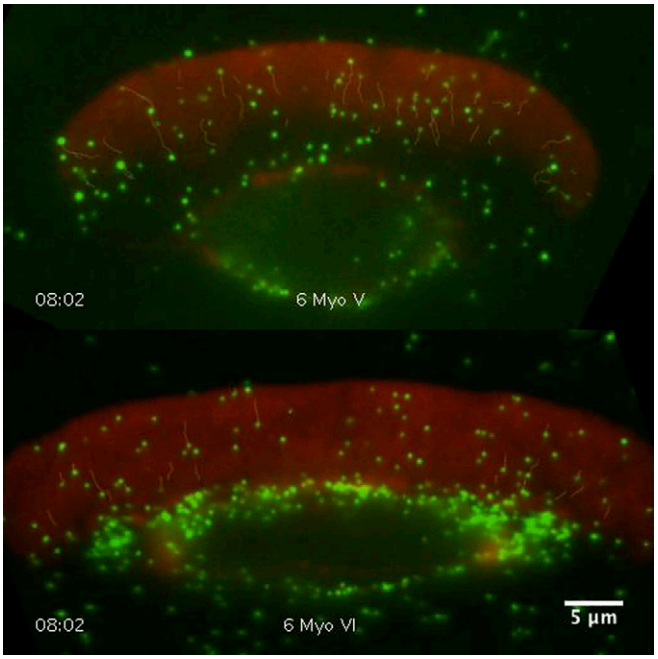

Movie S1. (*Upper*) Movie of scaffolds with 6 myosin V (green) meandering on a keratocyte actin network (red) (Fig. 3*C*). (*Lower*) Scaffolds with 6 myosin VI (green) moving linearly on the 2D network (Fig. 3*D*). Data were acquired at a 2-Hz frame rate, 2 mM ATP, and at room temperature.

Movie S1

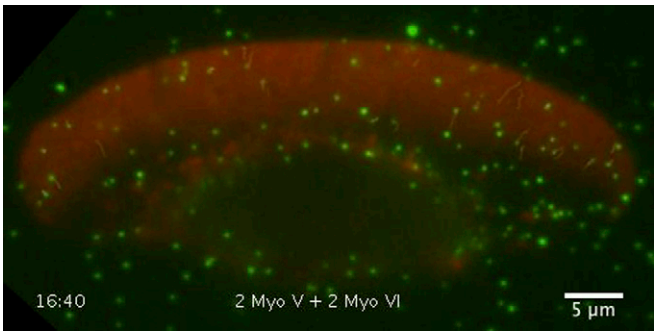

Movie S2. Scaffolds with 2 myosin V and 2 myosin VI meandering on a keratocyte actin network (red) (Fig. 6*A*). Scaffolds travel unidirectionally, either toward the cell periphery or the cell center. Data collected at a 2-Hz frame rate, 2 mM ATP, and at room temperature.

Movie S2